



LINKING DENSE GAS FROM THE MILKY WAY TO EXTERNAL GALAXIES

IAN W. STEPHENS¹, JAMES M. JACKSON¹, J. SCOTT WHITAKER², YANETT CONTRERAS³, ANDRÉS E. GUZMÁN⁴, PATRICIO SANHUEZA^{2,5}, JONATHAN B. FOSTER^{1,6}, AND JILL M. RATHBORNE³¹ Institute for Astrophysical Research, Boston University, Boston, MA 02215, USA; ianws@bu.edu² Physics Department, Boston University, Boston, MA 02215, USA³ Australia Telescope National Facility, CSIRO Astronomy and Space Science, Epping, NSW, Australia⁴ Departamento de Astronomía, Universidad de Chile, Camino el Observatorio 1515, Las Condes, Santiago, Chile⁵ National Astronomical Observatory of Japan, 2-21-1 Osawa, Mitaka, Tokyo 181-8588, Japan⁶ Yale Center for Astronomy and Astrophysics, New Haven, CT 06520, USA

Received 2015 December 18; accepted 2016 March 28; published 2016 June 8

ABSTRACT

In a survey of 65 galaxies, Gao & Solomon found a tight linear relation between the infrared luminosity (L_{IR} , a proxy for the star formation rate) and the HCN(1–0) luminosity (L_{HCN}). Wu et al. found that this relation extends from these galaxies to the much less luminous Galactic molecular high-mass star-forming clumps (~ 1 pc scales), and posited that there exists a characteristic ratio $L_{\text{IR}}/L_{\text{HCN}}$ for high-mass star-forming clumps. The Gao–Solomon relation for galaxies could then be explained as a summation of large numbers of high-mass star-forming clumps, resulting in the same $L_{\text{IR}}/L_{\text{HCN}}$ ratio for galaxies. We test this explanation and other possible origins of the Gao–Solomon relation using high-density tracers (including HCN(1–0), $\text{N}_2\text{H}^+(1-0)$, $\text{HCO}^+(1-0)$, HNC(1–0), $\text{HC}_3\text{N}(10-9)$, and $\text{C}_2\text{H}(1-0)$) for ~ 300 Galactic clumps from the Millimetre Astronomy Legacy Team 90 GHz (MALT90) survey. The MALT90 data show that the Gao–Solomon relation in galaxies cannot be satisfactorily explained by the blending of large numbers of high-mass clumps in the telescope beam. Not only do the clumps have a large scatter in the $L_{\text{IR}}/L_{\text{HCN}}$ ratio, but also far too many high-mass clumps are required to account for the Galactic IR and HCN luminosities. We suggest that the scatter in the $L_{\text{IR}}/L_{\text{HCN}}$ ratio converges to the scatter of the Gao–Solomon relation at some size-scale $\gtrsim 1$ kpc. We suggest that the Gao–Solomon relation could instead result from a universal large-scale star formation efficiency, initial mass function, core mass function, and clump mass function.

Key words: galaxies: star formation – ISM: clouds – ISM: molecules – stars: formation – stars: massive

Supporting material: machine-readable table

1. INTRODUCTION

The Kennicutt–Schmidt law (Schmidt 1959, 1963; Kennicutt 1998a, 1998b) describes an empirical relation between the surface density of star formation, Σ_{SFR} , and the surface density of gas, Σ_{gas} , in the form $\Sigma_{\text{SFR}} \propto (\Sigma_{\text{gas}})^N$. By tracing gas in normal spiral and starburst galaxies with $\text{H}\alpha$, H I , and $\text{CO}(1-0)$, N (commonly referred to as the Schmidt index) was found to be 1.4 ± 0.15 . Stars, however, form in dense clumps (size scales of ~ 1 pc) in giant molecular clouds (GMCs). While the gas mass of GMCs is best traced by CO , the dense clumps are better traced by molecules with higher dipole moments, such as HCN and HCO^+ , since these molecules are collisionally excited into emission only at higher densities. Gao & Solomon (2004, henceforth, GS04) investigated the Kennicutt–Schmidt law using the high-density tracer HCN(1–0) in normal galaxies, luminous infrared galaxies (LIRGs), and ultraluminous infrared galaxies (ULIRGs). Specifically, GS04 summed the fluxes across entire galaxies to calculate the HCN(1–0) luminosity (L_{HCN}) and the infrared (IR) luminosity (L_{IR} , as derived from the *Infrared Astronomical Satellite*, i.e., *IRAS*). The luminosities L_{IR} and $L_{\text{HCN}(1-0)}$ have a tighter power-law correlation than L_{IR} and $L_{\text{CO}(1-0)}$. Remarkably, the relations have significantly different power laws; while $L_{\text{IR}} \propto L_{\text{CO}(1-0)}^{1.4}$ (i.e., follows the Schmidt index $N = 1.4$), $L_{\text{IR}} \propto L_{\text{HCN}(1-0)}^{1.00 \pm 0.05}$. Specifically, GS04 found the empirical power-law $\log L_{\text{IR}} = 1.00 \log L_{\text{HCN}} + 2.9$, where L_{IR} is the *IRAS* IR luminosity in units of L_{\odot} and L_{HCN} is the HCN(1–0) luminosity in units of $\text{K km s}^{-1} \text{pc}^2$. This relation

will henceforth be called the Gao–Solomon relation. Narayanan et al. (2005) investigated the same relation with $\text{CO}(3-2)$ rather than HCN(1–0) and found a roughly consistent power-law $L_{\text{CO}(3-2)} \propto L_{\text{IR}}^{0.92 \pm 0.07}$.

Wu et al. (2005, henceforth, Wu05) observed HCN(1–0) for ~ 50 Galactic star-forming clumps, most of which are forming high-mass stars. When they compared these Galactic clumps (~ 1 pc scale) to the galaxies of GS04, they found that the Gao–Solomon relation extends over several orders of magnitude to these Galactic clumps. A similar result was found for dense gas within molecular clouds (Lada et al. 2012). A preliminary study based on the Millimetre Astronomy Legacy Team 90 GHz (MALT90) survey confirmed the Wu05 results (Jackson et al. 2013). The interpretation set forth by Wu05 was that the extragalactic luminosities L_{IR} and $L_{\text{HCN}(1-0)}$ could be explained as a summation of the luminosities of all high-mass star-forming clumps within a galaxy. Wu05 also suggested that the relation no longer holds for clumps with L_{IR} below $10^{4.5} L_{\odot}$ —approximately the luminosity of an ultracompact H II region. They suggested that clumps below this luminosity may not contain high-mass stars and therefore do not sample the complete initial mass function (IMF).

Krumholz & Thompson (2007) suggested that, given a turbulent medium, the relation between L_{IR} and a molecular line’s luminosity depends on the transition’s critical density and the median density of a galaxy. For the relation $L_{\text{IR}} \propto L_{\text{molecule}}^{\alpha}$, lines with critical densities lower than a galaxy’s median density of star-forming clouds, such as $\text{CO}(1-0)$, will have α equal to

the Schmidt index N . In contrast, lines with critical densities higher than this median density, such as HCN(1–0), will have $\alpha < N$. Narayanan et al. (2008) took a different approach to analyze the relation via 3D hydrodynamic simulations and found similar results as Krumholz & Thompson (2007). They also predicted α for higher J rotational transitions of CO and HCN. HCN(3–2), for example, is expected to have $\alpha \approx 0.7$. HCN(3–2) observations of galaxies follow $\alpha \sim 0.8$ (Bussmann et al. 2008; Graciá-Carpio et al. 2008; Juneau et al. 2009). Using observations of Galactic star-forming clumps, Wu et al. (2010, henceforth, Wu10) found that HCN(3–2) has $\alpha = 0.88 \pm 0.06$, significantly lower than that for HCN(1–0) observations ($\alpha = 1.07 \pm 0.06$), but still higher than that predicted for galaxies in Narayanan et al. (2008).

The physical basis for the Gao–Solomon relation is still under debate. Wu05 and Wu10 suggested that if the clump samples the high-mass regime of the stellar IMF, the clump will have a characteristic value of $L_{\text{IR}}/L_{\text{HCN}}$ (a proxy measurement for $L_{\text{IR}}/M_{\text{dense}}$, where M_{dense} is the dense gas mass). Summing large numbers of clumps with this characteristic value will preserve a linear relation from the clump-scale to the galaxy-scale. Krumholz & Thompson (2007), however, suggested that such a relation will occur over a large continuous distribution of interstellar medium structures given a universal star formation efficiency. A better understanding of the physical basis for the Gao–Solomon relation can be achieved by increasing the Galactic sample size of Wu05 and Wu10 and by observing other molecules that also trace high densities. The MALT90 survey (Foster et al. 2011, 2013; Jackson et al. 2013) targeted over 3000 star-forming clumps identified in the ATLASGAL 870 μm continuum survey (Schuller et al. 2009), simultaneously observing 16 lines near 90 GHz. Approximately 85% of these clumps surveyed have masses above $200 M_{\odot}$ (Y. Contreras 2016, in preparation), and clumps above $200 M_{\odot}$ are likely to form high-mass stars (e.g., Jackson et al. 2013). Thus, the MALT90 survey can test the relation between L_{IR} and molecular line luminosity with a much larger sample of high-mass star-forming clumps than the Galactic sample of ~ 50 clumps studied by Wu05.

In this paper, we investigate the Gao–Solomon relation using ~ 300 clumps that were covered by the MALT90 survey. We investigate the relation in a similar manner as GS04, Wu05, and Wu10, which compares the IR luminosity calculated from *IRAS* fluxes with the molecular line luminosity. In Section 2 we discuss the data used and the calculations of IR and molecular line luminosities. In Section 3, we discuss the Gao–Solomon relation, concentrating only on the HCN(1–0) molecular line. Specifically, we find that the Gao–Solomon relation does not seem to be well explained by a summation of high-mass clumps, and we discuss other possible origins of IR and HCN(1–0) emission and the Gao–Solomon relation itself. In Section 4 we discuss the Gao–Solomon relation with respect to the other dense gas tracers that were covered by the MALT90 survey. In Section 5 we discuss the implications of our analysis, and in Section 6 we summarize the results.

2. DATA AND METHODOLOGY

MALT90 mapped 16 lines for 3246 clumps, primarily high-mass star-forming clumps that are $>200 M_{\odot}$ (Jackson et al. 2013), as identified from the ATLASGAL survey. Many of these clumps had two velocity components separated significantly in velocity, indicating two unrelated clumps along

Table 1
Spectral Lines Covered by the MALT90 Survey

Species	Main Transition	Frequency (GHz)
N_2H^+	$J = 1 - 0$	93.173772
^{13}CS	$J = 2 - 1$	92.494303
H	41α	92.034475 ^a
CH_3CN	$J_K = 5_1 - 4_1$	91.985313
HC_3N	$J = 10 - 9$	90.979020
$^{13}\text{C}^{34}\text{S}$	$J = 2 - 1$	90.926036 ^a
HNC	$J = 1 - 0$	90.663572
HC^{13}CCN	$J = 10 - 9, F = 9 - 8$	90.593059 ^a
HCO^+	$J = 1 - 0$	89.188526
HCN	$J = 1 - 0$	88.631847
HNCO	$J_{K_a, K_b} = 4_{1,3} - 3_{1,2}$	88.239027 ^a
HNCO	$J_{K_a, K_b} = 4_{0,4} - 3_{0,3}$	87.925238
C_2H	$N = 1 - 0, J = \frac{3}{2} - \frac{1}{2},$ $F = 2 - 1$	87.316925
HN^{13}C	$J = 1 - 0$	87.090859
SiO	$J = 2 - 1$	86.847010
H^{13}CO^+	$J = 1 - 0$	86.754330

Note.

^a These are spectral lines that were not used in this study.

the line of sight. The MALT90 catalog (J. Rathborne 2016, in preparation) considers sources that have two velocity components separated by more than 15 km s^{-1} as two separate clumps, which brings the MALT90 catalog to a total of 3556 clumps (J. Rathborne 2016, in preparation). From henceforth, we will refer to one of these 3556 clumps as a “MALT90 clump.” In Table 4, these velocity-separated clumps are indicated using “_A” and “_B” suffixes. Clumps with the suffix “_S” are sources that do not have multiple velocity components separated by 15 km s^{-1} .

The lines observed with the MALT90 survey are given in Table 1. The antenna temperature, T_A^* , for all fluxes were converted to main beam temperature via $T_{\text{mb}} = T_A^*/\eta_{\text{mb}}$ where the main beam efficiency η_{mb} is taken to be 0.5 (Ladd et al. 2005). For brevity in the rest of the paper, we will not show the transitions for the molecules, and the transitions indicated in Table 1 will be referred to by the name of the molecule unless otherwise specified. Maps of the MALT90 survey are all lightly smoothed so that the FWHM beam size is $\theta_{\text{beam}} = 37''.8$ at all frequencies.

In this paper, we will define high-mass clumps to have masses $>200 M_{\odot}$, which are likely to form stars with masses $>8 M_{\odot}$ (Jackson et al. 2013), and define any clump $<200 M_{\odot}$ as a low-mass star-forming clump.

2.1. Calculation of Infrared Luminosity and Molecular Line Luminosity for MALT90 Clumps

In order to compare luminosities derived from *IRAS* (L_{IR}) to molecular line luminosities from MALT90 (L_{molecule}), we first matched the MALT90 clumps to the *IRAS* Point Source Catalog v2.1 (PSC). Although the MALT90 survey covered 3556 clumps, not all of these clumps have a corresponding *IRAS* source since compact sources may be extremely beam diluted and the wavelengths probed by *IRAS* are too short to probe the coldest clumps. In matching MALT90 clumps to *IRAS* sources, we required that the position of the MALT90 clump is within $0''.005$ ($18''$; approximately half the size of the

MALT90 beam) of the *IRAS* point source position. This cutoff was chosen since larger separations often include *IRAS* sources that are not associated with the MALT90 clump, and smaller separations remove sources that are associated with each other.

Following [GS04](#), [Wu05](#), and [Wu10](#), we used the standard formula to calculate L_{IR} from *IRAS* fluxes ([Sanders & Mirabel 1996](#))

$$L_{\text{IR}} = 0.56D^2(13.48f_{12} + 5.16f_{25} + 2.58f_{60} + f_{100}), \quad (1)$$

where L_{IR} is in L_{\odot} , distance D is in kpc, and f_x is the flux of the x μm *IRAS* band in Jy. This equation assumes a single temperature dust emissivity model. For dust temperatures in the range of 25–65 K, the luminosity should be accurate within 5% ([Sanders & Mirabel 1996](#)). Kinematic distances for L_{IR} (and L_{HCN} , see below) were calculated based on the clump velocity and solving for the near/far ambiguity, which will be presented in a future paper ([J. Whitaker et al. 2016](#), in preparation).

In order to calculate line luminosities of MALT90 clumps with the same methodology used in [Wu05](#) and [Wu10](#), for each line we fit each *IRAS*-matched MALT90 integrated intensity (moment 0) map with an elliptical Gaussian. We associated 405 MALT90 clumps with an *IRAS* source; a large fraction of the MALT90 clumps are cold ([Guzmán et al. 2015](#)), beam diluted with the *IRAS*, or distant and thus are undetected with *IRAS*. A MALT90 map is typically $4' \times 4'$ (27×27 pixels of size $9'' \times 9''$), but the outer $0.5'$ of the maps are noisier since the edges of the map have significantly less integration time due to the Mopra on-the-fly mapping procedure. Therefore, our fitting routine only considers the inner 75% of the pixels in each dimension (i.e., $\sim 3' \times 3'$) for each MALT90 map. The fitting routine also required that there be at least 5 pixels across the entire map with a signal-to-noise greater than 6. After all moment 0 maps were fit with an elliptical Gaussian, we manually inspected each fit overlaid on the moment 0 maps to judge whether the elliptical Gaussian provided a reasonable fit. Fits were removed if: (1) the map was significantly noisy, typically due to observations in poor weather that resulted in bad baselines; (2) a large portion ($\gtrsim 20\%$) of the elliptical Gaussian's FWHM extended beyond the map boundaries; (3) multiple peaks in the MALT90 map led to poor elliptical Gaussian fits; (4) the centroid of the elliptical Gaussian fit was $\gtrsim 2'$ from the clump and thus not likely to be associated with the *IRAS* source; (5) a MALT90 clump corresponded with two *IRAS* sources; or (6) the emission within the MALT90 map was too smooth and extended to allow for a proper elliptical Gaussian fit. Of the 405 *IRAS*-matched MALT90 clumps, 282 clumps had a valid flux for at least one line. Twelve of the sixteen spectral lines are presented in this paper. HNC0 ($4_{1,3}-3_{1,2}$), $\text{HC}^{13}\text{CCN}(J=10-9, F=9-8)$, and $^{13}\text{C}^{34}\text{S}(2-1)$ had no valid elliptical Gaussian fits and $\text{H}41\alpha$ is not a molecular line and had only three valid elliptical Gaussian fits.

Given the elliptical Gaussian fit of a map, we can calculate the integrated intensity in a similar manner as [GS04](#). We follow the equation given in [Wu05](#) and [Wu10](#)

$$L_{\text{molecule}} = 23.5 \times 10^{-6} D^2 \frac{\pi \theta_s^2}{4 \ln 2} \frac{\theta_s^2 + \theta_{\text{beam}}^2}{\theta_s^2} \int T_{\text{mb}}^* dv = 23.5 \times 10^{-6} D^2 \frac{\pi \theta_{\text{fit}}^2}{4 \ln 2} \int T_{\text{mb}}^* dv, \quad (2)$$

where L_{molecule} is in units of $\text{K km s}^{-1} \text{pc}^2$, D is in kpc, θ_s and θ_{beam} is the actual (deconvolved) angular size of the source and the angular of the beam, respectively, in arcseconds, and $\int T_{\text{mb}}^* dv$ is the peak velocity-integrated intensity in units of K km s^{-1} . $\theta_s^2 + \theta_{\text{beam}}^2$ is equal to the Gaussian fit size, which is approximated to be $\theta_{\text{fit}} = \sqrt{\theta_{\text{maj}} \times \theta_{\text{min}}}$, where θ_{maj} and θ_{min} are the FWHM sizes of the major and minor axis of the elliptical Gaussian fit.

The results of the elliptical Gaussian fits are given in Table 4. In this table, we only show fluxes for the MALT90 clumps rather than luminosities since certain clumps do not have valid kinematic distances. The fluxes reported in this paper are simply the luminosities divided by the square of the distance in kpc^2 , i.e.,

$$F_{\text{IR}} = 0.56(13.48f_{12} + 5.16f_{25} + 2.58f_{60} + f_{100}), \quad (3)$$

$$F_{\text{molecule}} = 23.5 \times 10^{-6} \frac{\pi \theta_{\text{fit}}^2}{4 \ln 2} \int T_{\text{mb}}^* dv, \quad (4)$$

where variables in these two equations are in the same units as Equations (1) and (2). The units for F_{IR} and F_{molecule} are therefore $L_{\odot} \text{kpc}^{-2}$ and $\text{K km s}^{-1} \text{pc}^2 \text{kpc}^{-2}$, respectively. The latter has both pc and kpc in the unit; we chose to keep the units in this format for easy conversion to luminosity by simply multiplying the fluxes by the square of the kpc distance D given in Column 3 of Table 4. F_{molecule} can be converted from $\text{K km s}^{-1} \text{pc}^2 \text{kpc}^{-2}$ to K km s^{-1} by multiplying by 10^{-6} .

Of the 282 clumps that had a valid flux for at least one line, 209 clumps also had a valid kinematic distance and thus have a luminosity for at least one line. Most of the clumps without a valid kinematic distance are those within 10° of the Galactic Center; kinematic distances within this longitude range cannot be calculated with high accuracy since a slight change in velocity can dramatically change a kinematic distance. Of these 209 clumps, 204 clumps had only one velocity component (i.e., has a suffix “_S” in Table 4). We only consider the molecular line luminosities for these 204 clumps throughout the paper.

2.2. Data from GS04 and Wu10

For the figures in this paper, we include data from [GS04](#) and [Wu10](#). From [Wu10](#), we do not include the clump DR21S since the value reported in their table for L_{HCN} is obviously errant (the value is too low for the reported flux, size, and distance of the source).

3. THE IR AND HCN LUMINOSITY CORRELATION FOR GALACTIC CLUMPS

Of the 204 *IRAS*-matched MALT90 clumps with valid luminosities for at least one line (see Section 2.1), 160 had valid HCN luminosities. In Figure 1, we show the Gao–Solomon relation along with the clumps from [Wu10](#) and MALT90 (this study). Like [Wu05](#), [Wu10](#), and [Jackson et al. \(2013\)](#), we find that the fit to the Gao–Solomon relation extends from the higher luminosities found in galaxies to the lower luminosities found in Galactic clumps.

3.1. The Clump Discrepancy

Based on any standard IMF (e.g., [Salpeter 1955](#); [Kroupa 2001](#)) and the fact that a star's luminosity is roughly proportional to the cube of its mass, it is easily shown that the

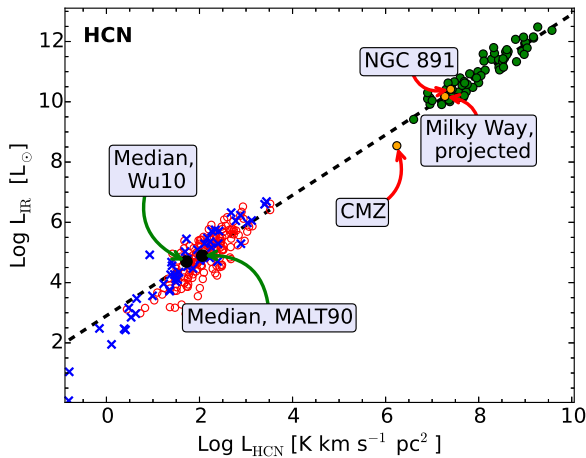


Figure 1. Gao–Solomon relation (L_{IR} vs. $L_{\text{HCN}(1-0)}$) shown for galaxies and Galactic clumps. Green circles are galaxies from GS04, blue crosses are Galactic clumps from Wu10, and red circles are MALT90 Galactic clumps presented in this paper. The black dashed line shows the original Gao–Solomon relation fit of $\log L_{\text{IR}} = 1.00 \log L_{\text{HCN}} + 2.9$, i.e., it is not fitting any of the Galactic sources. The relation extends from galaxies to Galactic clumps. The median values for the Wu10 and MALT90 clumps are indicated, as well as NGC 891. We show the projected location of the Milky Way assuming $L_{\text{IR}} = 1.5 \times 10^{10} L_{\odot}$ (Cox et al. 1986) and that the Milky Way follows the Gao–Solomon relation. We also show the location of the Central Molecular Zone (CMZ) with intensities integrated over the solid angle subtended by the Mopra CMZ 3 mm Band Survey discussed in Section 3.1.1.

stellar mass in galaxies is dominated by the low-mass stars, while the stellar luminosity is dominated by the high-mass stars. Wu05 and Wu10 suggested that the same low- and high-mass comparison for stars does not necessarily apply to dense gas mass and IR luminosity. Wu10 compared the HCN luminosity to the virial mass (M_{vir}), calculating the latter from the HCN spatial size and the linewidth of C^{34}S (5–4). The power-law relation for $L_{\text{IR}} \propto M_{\text{vir}}^{\gamma}$ might be expected to have γ near 2 since $L_{\text{IR}} \propto D^2$ and $M_{\text{vir}} \propto D$, where D is the distance to the source. However, empirically Wu10 find γ is ~ 1 . M_{vir} can be considered as a measure of the dense gas mass of a clump, M_{dense} . From these relations, they suggested that constant $L_{\text{IR}}/L_{\text{HCN}}$ is simply a reflection of a constant $L_{\text{IR}}/M_{\text{dense}}$.

The infrared luminosity of the Milky Way is estimated to be $L_{\text{IR}} \approx 1.5 \times 10^{10} L_{\odot}$ (Cox et al. 1986). While there is considerable difficulty in measuring the infrared luminosity of the Milky Way since it cannot be observed externally, this number is reasonable since NGC 891, an edge-on galaxy that strongly resembles the Milky Way, has a similar *IRAS* infrared luminosity of $2.6 \times 10^{10} L_{\odot}$ (GS04). If the Milky Way follows the Gao–Solomon relation, L_{HCN} would be $\sim 10^{7.3} \text{ K km s}^{-1} \text{ pc}^2$. For HCN, the mean and median MALT90 clump luminosity is $L_{\text{HCN}} = 10^{2.1} \text{ K km s}^{-1} \text{ pc}^2$ (Figure 1). If all high-mass clumps are approximately this luminosity, in order for high-mass clumps to sum up to the entire Milky Way L_{IR} , $\sim 150,000$ high-mass clumps are needed.

Alternatively we can estimate the number of high-mass clumps in the Galaxy if we assume that all dense gas in the Milky Way is contained within these clumps. Battisti & Heyer (2014) found that the ratio between the dense gas mass, M_{dense} , and the total molecular gas mass, $M_{\text{molecular}}$, is $M_{\text{dense}}/M_{\text{molecular}} = 0.07^{+0.13}_{-0.05}$. The molecular gas mass of the Milky Way is $\sim 2 - 3 \times 10^9 M_{\odot}$ (Combes 1991), suggesting a dense gas mass of $\sim 2 \times 10^8 M_{\odot}$. A typical high-mass star-

forming clump mass is $\sim 1000 M_{\odot}$ (e.g., Y. Contreras et al. 2016, in preparation), suggesting that if all dense gas are in these high-mass clumps, there would be 200,000 of these clumps. This estimate of the number of clumps is similar to the estimate based on the Gao–Solomon relation above.

These two estimates suggest that if dense gas is primarily contained within high-mass star-forming clumps, there are on order 10^5 high-mass star-forming clumps. However, the current estimates for the total number of such clumps in the Galaxy is much lower. For example, Zinnecker & Yorke (2007) suggest that only ~ 5400 high-mass stars in the Milky Way are in their accretion phase, yet these stars presumably reside in the clumps that are the brightest with *IRAS*. Moreover, the ATLASGAL survey is sensitive to all high-mass star-forming clumps with masses $> 200 M_{\odot}$ out to a distance of 10 kpc (5σ detections) (Schuller et al. 2009; Jackson et al. 2013), implying detections for almost all clumps $> 1000 M_{\odot}$ in the surveyed region (420 sq. degrees over $-80^\circ < l < +60^\circ$). Only $\sim 10,000$ total clumps were detected by ATLASGAL (Contreras et al. 2013; Csengeri et al. 2014; Urquhart et al. 2014) and many have masses below $1000 M_{\odot}$ (Y. Contreras 2016, in preparation); while the survey did not completely sample the Galaxy, it surveyed the inner galaxy where most of the molecular mass is present. Therefore, the number of massive clumps $> 1000 M_{\odot}$ is not likely to be significantly higher than $\sim 10,000$.

This analysis suggests that a significant amount of HCN emission from the Galaxy may not originate from dense, high-mass Galactic clumps. The same comparison can be drawn for the infrared luminosity. The mean and median MALT90 clump infrared luminosity is $L_{\text{IR}} = 10^{4.9} L_{\odot}$ (Figure 1). For a Milky Way luminosity of $L_{\text{IR}} = 1.5 \times 10^{10} L_{\odot}$ (Cox et al. 1986), if dense clumps emit all the infrared luminosity at this average value, 190,000 clumps are needed, well above the expected number of Galactic high-mass clumps. Therefore, a significant amount of infrared emission from the Galaxy cannot originate from dense, high-mass Galactic clumps.

In Figure 1, the scatter for the Galactic clumps is much larger than the scatter for galaxies from GS04. Part of the reason that the Galactic clumps may seem significantly correlated is due to the fact that both axes depend on the square of the distance which can cause the luminosities (L_{IR} and L_{HCN}) to be intrinsically correlated. Therefore, in Figure 2 we show the relation for fluxes F_{HCN} versus F_{IR} . Included in this plot are the GS04 galaxies, the Wu10 Galactic clumps, and the MALT90 Galactic clumps. We also have included in the plot an additional 51 MALT90 clumps that did not have valid distances but still have valid fluxes. For the GS04 galaxies, we multiplied the fluxes by the volumetric scale factor $(1+z)^3$. Note that the redshifts z for most GS04 galaxies are very small, and the overall relation is unaffected by this factor. This plot shows that the GS04 sources follow a different slope than the Galactic clumps. Additionally, most of the Wu10 clumps with luminosities over $10^{4.5} L_{\odot}$ lie above the best-fit line for the GS04 galaxies. This plot indicates that the extension to Galactic clumps may not be as tight of a relation as initially thought.

In summary, if the Gao–Solomon relation can be interpreted as beam-averaging typical high-mass star-forming clumps, then the number of clumps available in a galaxy appears to be insufficient by about an order of magnitude. Henceforth, we will call this mismatch between the estimated number of high-mass star-forming clumps and total luminosity of the Milky

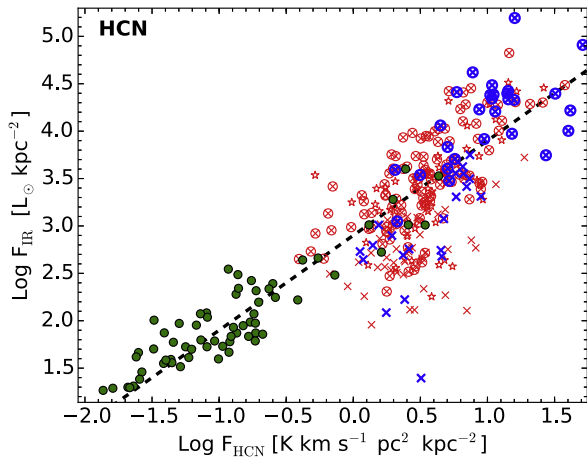


Figure 2. Plot of F_{IR} and F_{HCN} for Galactic clumps and galaxies. Green circles are galaxies from GS04, blue crosses are Galactic clumps from Wu10 (with blue circles indicating if $L_{\text{IR}} > 10^{4.5} L_{\odot}$), and red circles are Galactic clumps from MALT90 (with circles indicating if $L_{\text{IR}} > 10^{4.5} L_{\odot}$ and stars indicating clumps with no kinematic distances). The dashed line shows the Gao–Solomon relation $\log F_{\text{IR}} = 1.00 \log F_{\text{HCN}} + 2.9$. Units for F_{HCN} are in $\text{K km s}^{-1} \text{pc}^2 \text{kpc}^{-2}$ rather than K km s^{-1} for easy conversion to luminosity.

Way as the “clump discrepancy.” Moreover, the F_{IR} versus F_{HCN} plot (Figure 2) provides evidence that the extension of the relation down to Galactic clumps may be poorer than suggested by the luminosity–luminosity plot. We investigate possible explanations for this clump discrepancy and the possible origin of the Gao–Solomon relation in the following subsections and summarize at the end.

3.1.1. Investigating whether the Brightest Clumps or the Central Molecular Zone (CMZ) Dominate the IR and HCN Luminosities

A possible reason for the apparent clump discrepancy is that the most luminous clumps dominate the luminosity of entire galaxies. For example, if the Galaxy contained 1000 clumps with an average L_{HCN} of $10^{4.3} \text{K km s}^{-1} \text{pc}^2$, the clump discrepancy would easily be accounted for. For the 160 clumps with valid HCN luminosities, the brightest clump has $L_{\text{HCN}} \approx 10^{3.5} \text{K km s}^{-1} \text{pc}^2$. Approximately 6000 of these clumps can account for the total estimated L_{HCN} for the Milky Way ($\sim 10^{7.3} \text{K km s}^{-1} \text{pc}^2$). Of the 160 IRAS-matched MALT90 clumps with valid HCN luminosities, only 5 clumps have $L_{\text{HCN}} > 1000 \text{K km s}^{-1} \text{pc}^2$. Therefore, if the MALT90 sample accurately samples the high-mass clumps of the Galaxy (as it should, given the longitude coverage), the brightest clumps cannot dominate the Galactic HCN luminosity. Likewise, since the median ratio $L_{\text{IR}}/L_{\text{HCN}}$ lies approximately on the Gao–Solomon relation for these clumps, they cannot dominate the Galactic IR luminosity either.

No kinematic distance for a MALT90 clump has been calculated for sources within $\pm 10^\circ$ of the Galactic Center since a small change in velocity can change distances dramatically. However, toward the center of the Galaxy, the so-called CMZ, a large quantity of molecular gas exists. About one quarter (95 of 405) of MALT90 clumps that coincide with an IRAS source lie within 10° of the Galactic Center. We therefore investigate whether the CMZ can contribute significantly to the total Galactic L_{HCN} , and if so, whether the emission comes directly from high-mass star-forming clumps.

With the Five College Radio Astronomical Observatory (FCRAO) 14 m telescope, Jackson et al. (1996) mapped the

central 4.3×0.5 of the Galaxy ($630 \times 73 \text{ pc}$ assuming a distance of 8.34 kpc, Reid et al. 2014). Within this area, Jackson et al. (1996) calculated the HCN luminosity as $L_{\text{HCN}} = 10^{6.5} \text{K km s}^{-1} \text{pc}^2$, which is approximately one-sixth of the luminosity expected for the projected Milky Way’s L_{HCN} of $10^{7.3} \text{K km s}^{-1} \text{pc}^2$. Therefore, while the CMZ does not dominate the total Galactic L_{HCN} , the CMZ contributes a significant fraction (about one-sixth) to the total Galactic L_{HCN} . Within the same area there are 352 MALT90 clumps (J. Rathborne et al. 2016, in preparation) and 821 ATLASGAL clumps (Csengeri et al. 2014). If we assume there are indeed 821 high-mass star-forming clumps in this region, the average luminosity of a clump must be $10^{3.6} \text{K km s}^{-1} \text{pc}^2$ in order to produce the total CMZ L_{HCN} . If we assign a Galactic Center distance of 8.34 kpc to all MALT90 clumps within 10° of the Galactic Center, the maximum L_{HCN} for any individual clump (excluding _A and _B clumps in Table 4) is $10^{3.26} \text{K km s}^{-1} \text{pc}^2$ (AGAL351.161+00.697_S). Since the highest HCN luminosity toward a Galactic Center clump is lower than the average HCN clump luminosity needed for clumps to dominate the total CMZ’s luminosity, areas outside these clumps must provide a significant contribution to the HCN luminosity. Similarly, Cox & Laureijs (1989) find that the total CMZ infrared luminosity is dominated by extended areas. Cox & Laureijs (1989) calculated a total infrared luminosity of $10^9 L_{\odot}$ in an area of $3^\circ \times 2^\circ$ about the Galactic Center and found that the compact sources only accounting for 10% of this luminosity.

We quantify L_{IR} and L_{HCN} within the same area of the CMZ. We use data from the Mopra CMZ 3 mm Band Survey (Jones et al. 2012), which covers the CMZ in a box with dimensions of 2.5×0.5 and centered at Galactic coordinates $l = 0.5$ and $b = 0^\circ$. We use this solid angle for calculating the CMZ L_{IR} and L_{HCN} . The available maps provide the antenna temperatures T_A^* in the CMZ, i.e., the maps have not been corrected for the beam efficiency. For HCN, we first integrate over velocity to create an integrated intensity (moment 0) map. We then integrate over solid angle via $L_{\text{HCN}} = D^2 I \Omega / \eta_{\text{mb}}$, where I is the velocity-integrated intensity and Ω is the solid angle. The main beam efficiency, η_{mb} , was taken to be 0.5, and the distance, D , was taken to be 8.34 kpc. $I \Omega$ is equivalent to the sum of the pixels in the integrated intensity map times the solid angle subtended by a pixel. In the same box as this survey, we also calculated L_{IR} as determined from IRAS using Equation (1). For the area covered by the Mopra CMZ 3 mm Band Survey, $L_{\text{HCN}} = 10^{6.24} \text{K km s}^{-1} \text{pc}^2$ and $L_{\text{IR}} = 10^{8.54} L_{\odot}$.

Figure 1 shows these derived CMZ IR and HCN luminosities. The data-point lies significantly below the regression fit from the Gao–Solomon relation, with a factor of 4.0 less than the expected L_{IR} given its L_{HCN} . To put this significance in perspective, only two of 65 GS04 galaxies is offset from the regression line by more than a factor of 3. The CMZ is very turbulent compared to the rest of the Galactic plane, which causes the Jeans mass to be much higher in the CMZ. Therefore, it is expected and known (e.g., Longmore et al. 2013) that there will be a surplus of gas per unit of star formation, i.e., a smaller ratio of $L_{\text{IR}}/L_{\text{HCN}}$. This discrepancy in L_{IR} in the CMZ would suggest that in order for the Milky Way to lie on the best-fit line of the Gao–Solomon relation, on average the rest of the Milky Way must have a higher ratio of $L_{\text{IR}}/L_{\text{HCN}}$ than determined by the Gao–Solomon relation. For example, if the CMZ makes up one-sixth of the entire Milky Way’s L_{HCN} and lies a factor of four below the Gao–Solomon

relation, the rest of the Milky Way has to be 15% above the Gao–Solomon relation in order for the entire Milky Way to follow the relation exactly. Different galaxies likely have different fractional quantities of HCN within their own CMZ, and these areas are subject to different conditions than the plane of a galaxy. Indeed, not all GS04 galaxies lie exactly on the regression fit, and it is conceivable that different quantities of gas and conditions within the CMZs of each galaxy can cause scatter in the Gao–Solomon relation. Future models probably should account for parameter differences toward the centers of galaxies (e.g., higher turbulence) when modeling the Gao–Solomon relation.

In summary, the brightest clumps cannot dominate the Galactic L_{HCN} and L_{IR} luminosities and thus account for the clump discrepancy. The CMZ, however, makes up a significant fraction ($\sim 10\%$ – 20%) of both the HCN and IR luminosity of the Milky Way, but the solid angle covered by the Mopra CMZ 3 mm does not follow the Gao–Solomon relation. Moreover, extended emission outside dense clumps appears to add a significant (and perhaps a dominant) component to the CMZ HCN and IR emission.

3.1.2. Investigating whether the Low-mass Star-forming Clumps Dominate the IR and HCN Luminosities

The apparent clump discrepancy could be resolved if low-mass clumps rather than high-mass clumps dominate a galaxy’s total L_{IR} and L_{HCN} . Indeed, the results in this paper primarily focus on bright, high-mass infrared clumps that are detected with *IRAS*. In this subsection, first we will address whether these low-mass clumps can dominate the total Galactic L_{HCN} , and then we will address whether they can dominate the total Galactic L_{IR} . The Galaxy’s total L_{HCN} and L_{IR} from low-mass star-forming clumps depend on the clump mass function (CIMF) and the relation between the mass of the clump and each luminosity.

We assume that the CIMF takes the typical form $dN/dM \propto M^{-\delta}$. The empirical value for δ vary significantly (values of 1.4–2.4, e.g., Elmegreen & Falgarone 1996; Kramer et al. 1998), although the more recent studies find $\delta \gtrsim 1.8$ (e.g., Schneider & Brooks 2004; Reid & Wilson 2006; Pekruhl et al. 2013). In the Carina nebula complex, Pekruhl et al. (2013) found that for clumps with masses between ~ 50 and $3000 M_{\odot}$, $\delta = 1.95 \pm 0.07$. δ depends on the input parameters and the clump finding algorithm, and Pekruhl et al. (2013) showed that using different temperatures or algorithms could result in values of δ from 1.89 ± 0.06 and 2.15 ± 0.08 . Observations and simulations by Reid & Wilson (2006) and Reid et al. (2010), respectively, found that the CIMF index is similar to the Salpeter (1955) stellar IMF index, i.e., $\delta = 2.35$. We will consider both $\delta = 1.8$ and 2.35 for our analysis.

The relation between L_{HCN} and the clump mass is also not well determined, especially in the low-mass regime, but observations from Wu10 suggest that L_{HCN} may be directly proportional to the virial mass M_{vir} . The Wu10 sample primarily consists of high-mass clumps ($M_{\text{vir}} \sim 10^2$ to $10^5 M_{\odot}$) but two low-mass clumps ($M_{\text{vir}} \sim 30$ and $100 M_{\odot}$) are also included and follow the same relation. We will assume L_{HCN} is proportional to M for our calculations.

Based on the CIMF and the $L_{\text{HCN}}-M_{\text{vir}}$ relation, we now determine the fractional contribution to a galaxy’s total L_{HCN} from low-mass and high-mass star-forming clumps. Clumps above $\sim 200 M_{\odot}$ are likely to form high-mass stars (e.g.,

Jackson et al. 2013). We assume the CIMF extends to the highest mass clumps with masses of $10^5 M_{\odot}$ (e.g., G0.253 +0.016, also known as the Brick, Longmore et al. 2012). The fractional L_{HCN} contribution from low-mass and high-mass star-forming clumps is strongly affected by our choice of the lower mass-limit of the CIMF. The simulation by Reid et al. (2010) suggests that δ is constant for clumps down to $\sim 2 M_{\odot}$. Observations are not typically complete enough to sample this low-mass regime, but Pekruhl et al. (2013) showed that δ appears to at least be constant down to $\sim 50 M_{\odot}$. We will assume that the CIMF extends down to $2 M_{\odot}$. Assuming $\delta = 1.8$, clumps between 2 and $200 M_{\odot}$ contribute approximately 25% of the HCN luminosity as clumps between 200 and $10^5 M_{\odot}$. Alternatively assuming $\delta = 2.35$, clumps between 2 and $200 M_{\odot}$ contribute approximately 4.5 times the HCN luminosity than clumps between 200 and $10^5 M_{\odot}$.

Given the uncertainties in this calculation, we cannot definitively determine whether high-mass or low-mass star-forming clumps contribute more significantly to a galaxy’s total L_{HCN} . However, we have shown that it is certainly feasible that low-mass star-forming clumps ($< 200 M_{\odot}$) can contribute up to a factor of ~ 5 more to the total L_{HCN} of a galaxy than high-mass star-forming clumps ($> 200 M_{\odot}$). Therefore, if high-mass star-forming clumps contribute approximately one tenth of a galaxy’s total L_{HCN} (such as our Galaxy, beginning of Section 3), low-mass star-forming clumps could contribute almost half of a galaxy’s total L_{HCN} . If high- and low-mass star-forming clumps combined contribute $\sim 60\%$ to the Galaxy’s L_{HCN} , and the Galactic Center’s L_{HCN} luminosity is added (approximately one sixth of the Galaxy’s total L_{HCN} , Section 3.1.1), $\sim 75\%$ of the Galaxy’s total HCN luminosity is accounted for.

Although low-mass star-forming clumps may dominate a galaxy’s total L_{HCN} , they are not likely to dominate the total galaxy’s L_{IR} . According to Wu10, clumps with luminosities L_{IR} are approximately directly proportional to M_{vir} for $L_{\text{IR}} > 10^{4.5} L_{\odot}$ and $M_{\text{vir}} > 500 M_{\odot}$. Clumps below $\sim 300 M_{\odot}$ tend to have an order of magnitude less L_{IR} per unit M_{vir} as those with $M_{\text{vir}} > 500 M_{\odot}$. Therefore, low-mass star-forming clumps probably do not dominate a galaxy’s total L_{IR} . The fact that low-mass star-forming clumps may dominate L_{HCN} but not L_{IR} indicates an excess of HCN per unit of infrared luminosity for low-mass star-forming regions. This excess of HCN emission is seen for clumps less than $L_{\text{IR}} < 10^{4.5}$ in Figures 1 and 2. These clumps are a mix of low-mass star-forming clumps and clumps at a younger evolutionary stage; the latter will be addressed in Section 4.1.

To further characterize the possible contribution of low-mass star-forming clumps to the Galactic HCN luminosity, we consider the well-known low-mass star-forming region Serpens Main. The CARMA interferometer has publicly available interferometric HCN(1–0) data of this region at $7''6$ resolution (Lee et al. 2014). These observations used the CARMA23 mode which recovers the zero-spacing flux. Assuming a distance of 415 pc (VLBA parallax observations, Dzib et al. 2010), Serpens Main consists of two sub-clumps of $97 M_{\odot}$ and $144 M_{\odot}$ (Olm & Testi 2002). From *IRAS*, we calculate L_{IR} luminosities of 60 and $123 L_{\odot}$, respectively, resulting in a total L_{IR} of $183 L_{\odot}$. Given L_{IR} of Serpens Main, the Gao–Solomon relation predicts L_{HCN} to be $0.23 \text{ K km s}^{-1} \text{ pc}^2$. However, fitting an elliptical Gaussian to the HCN emission of Serpens Main results in

$L_{\text{HCN}} = 180 \text{ K km s}^{-1} \text{ pc}^2$ for the entire complex—almost 3 orders of magnitude higher than expected by the Gao–Solomon relation. Only $\sim 10^5$ low-mass star-forming clumps like Serpens Main are required to produce the HCN luminosity of the entire Milky Way, which is certainly a plausible number of these clumps given that there may be approximately 10^4 high-mass star-forming clumps (Section 3.1).

In summary, while low-mass star-forming clumps are not likely to contribute a significant fraction to the total Galactic L_{IR} , these clumps may contribute significantly to the total Galactic L_{HCN} .

3.1.3. Investigating whether Subthermal Emission of HCN Dominates the HCN Luminosity

The apparent clump discrepancy could be resolved if diffuse HCN emission not associated with dense clumps contributes significantly to the total HCN luminosity of the Milky Way. The HCN rotational level $J = 1$ is easily populated for even cold gas since the temperature difference between the $J = 1$ and the $J = 0$ ground state is only 4.3 K. Although collisional excitation plays the most important role for HCN emission in regions above the HCN critical density, below this density HCN radiative excitation dominates. Excitation below the critical density is typically called subthermal excitation because the excitation temperature is lower than the kinetic temperature. All lines observed in the MALT90 survey have critical densities $> 10^5 \text{ cm}^{-3}$, and thus these molecular transitions are ideal for locating dense clumps associated with star formation. Outside of these dense clumps, HCN emission is expected to be primarily subthermal. The subthermally emitting HCN molecules are still subject to collisions, allowing for HCN(1–0) emission above the background temperature.

Helfer & Blitz (1997) observed CO(1–0) and the high-density tracers HCN(1–0) and CS(2–1) in an unbiased survey of the Galactic plane at $\sim 1'$ resolution with the NRAO 12 m telescope. Between Galactic longitudes $l = 15^\circ.5$ and $l = 55^\circ.5$, they pointed the telescope in equally spaced increments of 1° . For almost every pointing, they detected all three lines. The integrated intensity ratios $I_{\text{HCN}}/I_{\text{CO}}$ and $I_{\text{CS}}/I_{\text{CO}}$ varied significantly from pointing to pointing. Each pointing generally detected lines with multiple velocity components, and the velocity components were typically at consistent velocities for all three molecular lines. Helfer & Blitz (1997) also mapped several GMCs and detected extended emission in CO(1–0), but only the dense clumps were detected in HCN(1–0) and CS(2–1). The typical integrated intensity ratios in their unbiased survey is $I_{\text{HCN}}/I_{\text{CO}} = 0.026$ and for clumps detected in GMCs, the ratio is $I_{\text{HCN}}/I_{\text{CO}} = 0.1$. Since $I_{\text{HCN}}/I_{\text{CO}}$ is much larger toward dense clumps than the 1° separated locations along the Galactic plane, Helfer & Blitz (1997) proposed that the HCN emission is likely to be subthermal with a typical ratio $I_{\text{HCN}}/I_{\text{CO}} = 0.026 \pm 0.008$. For NGC 891, a galaxy considered very similar to the Milky Way, GS04 measured $I_{\text{HCN}}/I_{\text{CO}}$ to be 0.024, which is almost identical to the Helfer & Blitz (1997) measurements for the Galactic plane. Therefore, if the unbiased survey of the Galactic plane is primarily detecting subthermal HCN emission, it is likely that the HCN luminosity in GS04 galaxies can also be dominated by subthermal emission.

Conversely, the model by Krumholz & Thompson (2007) showed that for HCN(1–0) emission, GMCs do not emit a significant fraction of their HCN luminosities at densities

$n \lesssim 10^4 \text{ cm}^{-3}$; instead, most of the luminosity is emitted from gas near the critical density. This model suggests that purely subthermal excitation does not account for the dominant emission of a galaxy’s HCN luminosity. Although Krumholz & Thompson (2007) made some simplified assumptions (e.g., densities follow a log-normal probability distribution function in molecular clouds), there appears to be a clear discrepancy between the results of Helfer & Blitz (1997) and Krumholz & Thompson (2007).

Given this apparent discrepancy between Helfer & Blitz (1997) and Krumholz & Thompson (2007), we further inspect the Helfer & Blitz (1997) study to analyze whether their data unequivocally show that the HCN emission from their Galactic plane survey is primarily subthermal. In Figure 3 we plot the $870 \mu\text{m}$ continuum data from ATLASGAL toward every Helfer & Blitz (1997) pointing. The red circle in each panel shows the FWHM of the NRAO 12 m beam ($71''$). In the top right of each figure, we indicate whether the HCN peak flux is $T_R^* < 0.05 \text{ K}$ (no X), $0.05 \text{ K} < T_R^* < 0.10 \text{ K}$ (white X), or $T_R^* > 0.10 \text{ K}$ (red X). While the integrated HCN intensity would give a better sense of the strongest HCN emission, this was not available in Helfer & Blitz (1997). In general, pointings with higher HCN peak fluxes have significant $870 \mu\text{m}$ continuum flux, especially fields that have HCN $T_R^* > 0.10 \text{ K}$ (red X). Note that even though HCN emission may not be coincident within the FWHM of the beam, the beam is Gaussian, allowing for the strong emission bordering the FWHM of the beam to contribute significantly to the detected flux for the HCN pointing.

The Helfer & Blitz (1997) argument that this HCN emission is subthermal because the $I_{\text{HCN}}/I_{\text{CO}}$ ratio is significantly different to the ratio observed in clumps may be errant. The exact same result would be found if the beams are instead not centered on the clumps (i.e., the HCN peaks) since CO emission in clouds is more uniform than HCN emission. This indeed appears to be the case since Figure 3 shows that the Helfer & Blitz (1997) pointings are typically offset from the continuum peaks. By comparing Figure 5 of Helfer & Blitz (1997) with Figure 3 here, it is evident that the beams more centered on strong $870 \mu\text{m}$ continuum emission (e.g., $l = 22^\circ.5$) have much higher $I_{\text{HCN}}/I_{\text{CO}}$ values than those with $870 \mu\text{m}$ emission along the border of the beam (e.g., $l = 30^\circ.5$). Moreover, the $870 \mu\text{m}$ continuum maps of the ATLASGAL survey appear filamentary, which likely indicates locations of elongated, dense structures rather than areas of subthermal emission. The multiple HCN velocity components detected in Helfer & Blitz (1997) could simply be explained by multiple clumps at different distances; for example, the fields centered at longitudes $22^\circ.5$, $23^\circ.5$, $30^\circ.5$, and $33^\circ.5$ obviously have multiple clumps in the field that could be at very different distances. Moreover, for the spectra in Helfer & Blitz (1997), the ratio $I_{\text{HCN}}/I_{\text{CO}}$ for velocity components within a single pointing vary significantly; for two clumps with different velocities, this would be expected if the beam is centered more on one clump than the other.

The integrated intensity ratio of the Helfer & Blitz (1997) Galactic plane survey ($I_{\text{HCN}}/I_{\text{CO}} = 0.026$) is still an important quantity even though there certainly is some contamination by clumps; since the survey is unbiased, the intensity ratio represents the expected intensity when beam-averaging the clumps throughout the plane of a galaxy similar to the Milky Way. This could explain why a similar integrated intensity ratio, i.e., $I_{\text{HCN}}/I_{\text{CO}} = 0.024$, was found for NGC 891 in GS04.

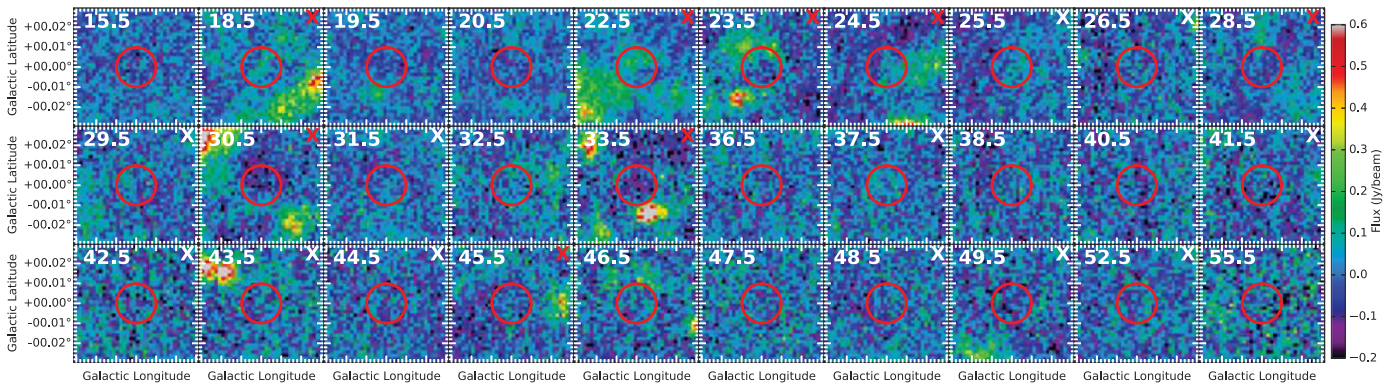


Figure 3. ATLASGAL (Schuller et al. 2009) $870\ \mu\text{m}$ emission (color-scale, $19''$ resolution) of the fields surveyed in Helfer & Blitz (1997). The white number in the top left of each panel indicates the Galactic longitude of the pointing. The $71''$ HCN beam is shown as a red circle in each panel. In general, each pointing is separated by a degree, although there are several pointings that Helfer & Blitz (1997) excluded due to poor data quality. In the top right corner of each figure, no “X” indicates an HCN peak radiative temperature $T_R^* < 0.05\ \text{K}$, a white “X” indicates $0.05\ \text{K} < T_R^* < 0.10\ \text{K}$, and a red “X” indicates $T_R^* > 0.10\ \text{K}$. Note that the noise in each ATLASGAL map is not always the same, e.g., the noise for the $l = 55.5$ map is higher than the other fields. Pointings that show significant HCN emission in Helfer & Blitz (1997) typically have significant nearby $870\ \mu\text{m}$ emission.

Although the Helfer & Blitz (1997) Galactic plane survey was sometimes coincident with clumps along the line of sight, a significant contribution to a galaxy’s total HCN emission may still come from subthermal HCN emission. For example, McQuinn et al. (2002) mapped a two square degree area in the Galactic plane with the high-density tracer CS(2–1) and found 3σ detections for $\sim 75\%$ of the solid angle covered. 85% of the 3σ detections comes from areas with no obvious clumps, suggesting these regions have subthermal-emitting gas. This supposed subthermal emission contributes $\sim 65\%$ to the total intensity within the two square degree map and thus dominates the emission in the region. Moreover, many extragalactic observations have suggested that subthermal emission of a high-density tracer can contribute significantly to the line luminosity of an entire galaxy (e.g., Papadopoulos 2007; Aravena et al. 2014).

In summary, measurements of previously reported Galactic subthermal emission from Helfer & Blitz (1997) is probably contaminated by clumps. The ratio of Galactic plane intensities found by Helfer & Blitz (1997), $I_{\text{HCN}}/I_{\text{CO}} = 0.026$, probably does not quantify the Galactic HCN contribution from only subthermal emission but rather the expected ratio observed in a plane of a galaxy similar to a Milky Way. However, based on other studies, it is possible that subthermal emission can contribute significantly to a galaxy’s total L_{HCN} . Diffuse gas with densities below the HCN critical density (i.e., subthermally excited) may dominate the total HCN luminosities from galaxies due to the much larger solid angle occupied by the diffuse gas compared to the solid angle occupied by dense clumps.

3.1.4. Investigating whether the Extended Emission due to the Interstellar Radiation Field (ISRF) Dominates the Infrared Luminosity

High-mass OB stars dominate the energy of the ISRF and the flux in *IRAS* bands. Cold dust ($\lesssim 25\ \text{K}$) is heated by the ISRF, warm dust ($\sim 30\text{--}40\ \text{K}$) is heated by young stellar populations, and hot dust ($\gtrsim 250\ \text{K}$) is heated by the general ISRF and OH/IR stars (Cox et al. 1986). Emission from all three dust components contribute significantly to the total IR flux. Given that the general ISRF includes contributions from both younger and older high-mass stellar populations, there may be significant contribution to the total Milky Way’s IR luminosity from dust not heated by embedded high-mass young stellar objects (YSOs). Extended, more diffuse regions, may be heated

by either the general ISRF or by photons escaping from young regions and thus may contribute a significant fraction to the total IR luminosity. Already we suggested this could be the case in the CMZ (Section 3.1.1).

To understand the infrared contribution from high-mass YSOs and extended IR emission to a galaxy’s total L_{IR} , it is helpful to inspect an external galaxy. The Large Magellanic Cloud (LMC) is perhaps the best example of a nearby galaxy that can be studied at high enough spatial resolution to resolve individual stars and YSOs. The LMC is located at 50 kpc (Feast 1999) and is nearly face-on (35° inclination with respect to the plane of sky, van der Marel & Cioni 2001). We present the $12\ \mu\text{m}$ *IRAS* images of the LMC in Figure 4. Overlaid on this image are the locations of *Spitzer*-identified high-mass YSOs (the “definite” and “probable” YSOs identified in Gruendl & Chu 2009), known OB associations (Lucke & Hodge 1970), and *IRAS* sources from the *IRAS* Point Source Catalog. Almost all Gruendl & Chu (2009) high-mass YSOs are at locations with strong $12\ \mu\text{m}$ *IRAS* emission, but many OB associations (i.e., high-mass star conglomerations that are not embedded) are not closely associated with any $12\ \mu\text{m}$ emission. Conversely, there are many areas with strong $12\ \mu\text{m}$ emission that do not have a high-mass YSO as identified by Gruendl & Chu (2009).

In the left panel of Figure 4, we also show the known GMCs in the LMC as probed by CO(1–0) with the NANTEN telescope (Fukui et al. 2008). This survey had a 3σ detection limit for molecular clouds with molecular hydrogen column density of $N(\text{H}_2) > 8 \times 10^{20}\ \text{cm}^{-2}$ (assuming a conversion factor X_{CO} of $7 \times 10^{20}\ \text{cm}^{-2}\ (\text{K km s}^{-1})^{-1}$). If we assume a minimum thickness of 1 pc for the GMCs along the line of sight (this value is conservatively low since the plane-of-sky extent of CO emission is typically much larger than this; Figure 4), a non-detection must have an average density within the NANTEN $2.6'$ beam of $n_{\text{H}_2} < 260\ \text{cm}^{-3}$. Nevertheless, there are large areas in the LMC that are bright with *IRAS* but have no detection of CO from NANTEN, indicating $N(\text{H}_2) < 8 \times 10^{20}\ \text{cm}^{-2}$ in these areas. This extended IR emission can reach scales of over 100 pc, and given the average column (and inferred volume) density at these scales, HCN will not be thermally excited.

In order to test whether this extended IR emission outside of the known CO(1–0) gas behaves according to the Gao–

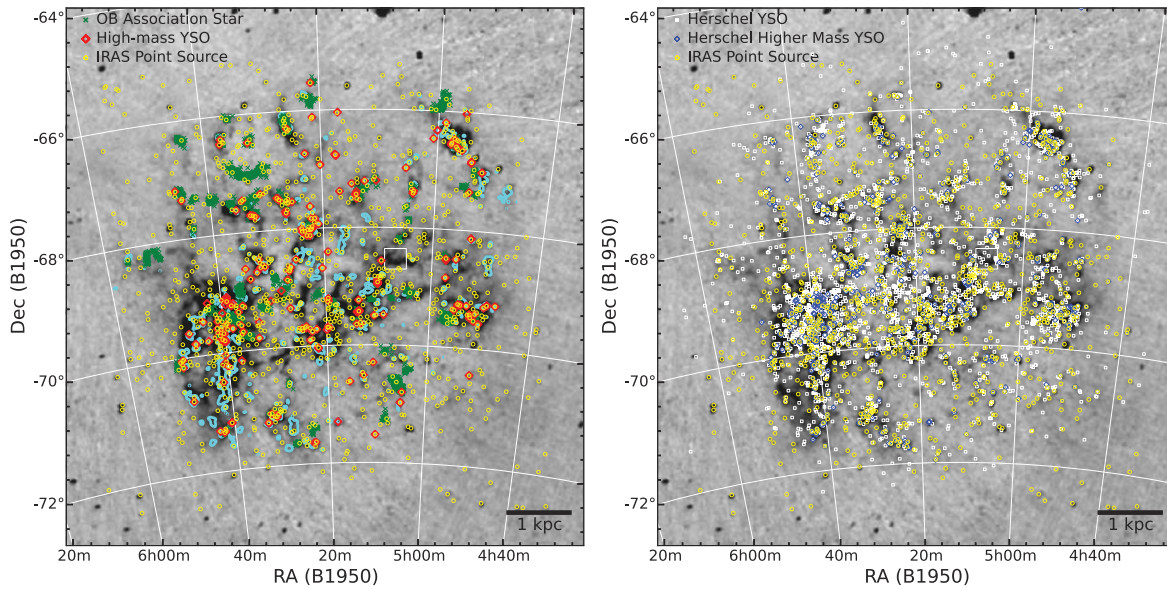


Figure 4. *IRAS* 12 μm images (grayscale) of the Large Magellanic Cloud. Left: the locations of high-mass young stellar objects (Gruendl & Chu 2009) are shown with red diamonds and OB stars of known OB associations (Lucke & Hodge 1970) are shown with green crosses. Sources from the *IRAS* Point Source Catalog are shown with yellow circles. Cyan contours are 3σ CO(1–0) detections from NANTEN (Fukui et al. 2008), indicating locations where the column density is $N(\text{H}_2) \gtrsim 8 \times 10^{20} \text{ cm}^{-2}$. The white rectangle shows a location where there is an *IRAS* detection but no *IRAS* point source, no Gruendl & Chu (2009) high-mass YSO, and no OB association stars. Right: the locations of known *Herschel* YSOs are in white and higher-mass YSOs (i.e., sources with *Herschel* luminosities $>1000 L_{\odot}$) are in blue. Like the left panel, we also show the *IRAS* point sources and a white rectangle for an area of interest.

Solomon relation, we select an area with *IRAS* emission void of any Fukui et al. (2008) CO(1–0) cloud, *IRAS* source, Gruendl & Chu (2009) YSO, and Lucke & Hodge (1970) OB association stars, as shown with the white box (size $20' \times 21'$, or $290 \times 305 \text{ pc}$) in both panels of Figure 4. The infrared luminosity in this box (using Equation (1)) is $L_{\text{IR}} = 10^{6.6} L_{\odot}$. If this region followed the Gao–Solomon relation, the HCN integrated intensity would be 2.1 K km s^{-1} . The CO(1–0) survey with NANTEN has a 3σ detection limit of $\sim 1.2 \text{ K km s}^{-1}$, yet CO, which is typically a factor of ~ 10 to 100 times brighter than HCN (e.g., Helfer & Blitz 1997), was completely undetected in this region. Therefore, this extended IR emission does not behave according to the Gao–Solomon relation.

We compare L_{IR} of the entire LMC ($L_{\text{IR,LMC,All}}$) and the sum of L_{IR} for all sources in the *IRAS* PSC ($L_{\text{IR,LMC,PSC}}$), and we find that $L_{\text{IR,LMC,PSC}}$ does not dominate $L_{\text{IR,LMC,All}}$. To calculate $L_{\text{IR,LMC,All}}$, we sum the flux for each *IRAS* band of the LMC about a 7.5×7.5 box centered at R.A. (B1950) = $5^{\text{h}}20^{\text{m}}$ and decl. = $-68^{\circ}50'$. From Equation (1) we find that $L_{\text{IR,LMC,All}} = 10^{9.1} L_{\odot}$. The sum of L_{IR} of all the *IRAS* point sources (shown as yellow circles in Figure 4) in the same box is $L_{\text{IR,LMC,PSC}} = 10^{8.2} L_{\odot}$. The *IRAS* point source catalog detects any LMC IR source with $L_{\text{IR}} \gtrsim 10^{3.1} L_{\odot}$, suggesting that all the high-mass star-forming regions ($L_{\text{IR}} \gtrsim 10^{4.5} L_{\odot}$) are detected. The sum of the point sources is only 12% of the entire LMC IR luminosity. As discussed at the beginning of Section 3, this 12% factor is similar to the fraction of L_{IR} that $\sim 10,000$ high-mass clumps are expected to contribute to the Milky Way’s total L_{IR} .

Since there are no known high-mass YSOs in some LMC extended IR regions, the IR emission probably comes from dust grains heated by the LMC’s ISRF (Cox et al. 1986). The HERITAGE *Herschel* survey (100–500 μm) of the LMC (Meixner et al. 2013) provides a much more complete catalog

of LMC IR sources (Seale et al. 2014) due to its higher sensitivity (especially for cold sources) and much higher resolution. In the right panel of Figure 4, we show the most probable YSOs in the LMC. Specifically, we chose all sources in the Seale et al. (2014) catalog that were considered as “probable” or “possible” YSOs as well as dust clump sources with luminosities $>1000 L_{\odot}$. Dust clumps that had luminosities $>1000 L_{\odot}$ have a very high chance of containing an embedded YSO since the luminosity of the dust clump cannot be explained by the LMC ISRF only (Seale et al. 2014). We also mark in Figure 4 the “higher mass” YSOs, which includes all Seale et al. (2014) sources (“probable” and “possible” YSOs and dust clumps) with luminosities $>1000 M_{\odot}$. Note that a small fraction of the bright YSOs and dust clumps in Seale et al. (2014) had *Herschel* fluxes that failed the SED fitting process and thus could not be labeled in the figure as a “higher mass” YSO. Most extended IR regions consist of at least one low-mass YSO, and these YSOs have insufficient luminosity to contribute significantly to the infrared luminosity of the entire cloud. This dust is more likely heated by the ISRF than embedded stars.

This analysis casts doubt on the interpretation put forth by Wu05 and Wu10. They proposed that above $L_{\text{IR}} > 10^{4.5} L_{\odot}$, star-forming molecular clumps have a roughly constant value of $L_{\text{IR}}/L_{\text{HCN}}$. The sum of the luminosities of large numbers of such clumps then produce the total L_{IR} and L_{HCN} of a galaxy, conserving the linear relation between L_{IR} and L_{HCN} . We have shown that a significant fraction of IR emission in the LMC comes from diffuse areas rather than *IRAS* clumps, and these areas probably do not follow the Gao–Solomon relation. A significant fraction of $L_{\text{IR,LMC,All}}$ likely comes from ISRF. Similar studies have also calculated the IR contribution from different components in the Milky Way. Mezger et al. (1982) showed that $\sim 80\%$ of the Galaxy’s far-infrared luminosity comes from low density regions, while only $\sim 10\%$ – 20% comes

from more compact sources. The extended emission is heated by approximately equal fractions from the ISRF and diffuse emission from low-density areas of H II regions (Cox & Laureijs 1989). Based on previous studies and our analysis here, we suggest that extended emission does not have a characteristic value $L_{\text{IR}}/L_{\text{HCN}}$ and likely dominates the total infrared luminosity of galaxies.

3.2. Summary of Origin of the Clump Discrepancy

We introduce the idea of a clump discrepancy, i.e., if high-mass clumps in a galaxy are units that sum to produce the observed $L_{\text{IR}}/L_{\text{HCN}}$ of an entire galaxy, then the Milky Way needs a factor of ~ 10 more high-mass star-forming clumps than are currently expected to exist to satisfy the Gao–Solomon relation. This suggests that the current estimates of the number of high-mass star-forming clumps in the Milky Way are either drastically wrong or some of the IR and HCN emission must originate outside high-mass clumps. We analyze four other possible origins of the missing L_{IR} and L_{HCN} within the Milky Way.

1. We first investigated whether the largest clumps or the CMZ could dominate L_{IR} or L_{HCN} in the Milky Way. The former appears unlikely given the current known population of clumps in the Galaxy. The CMZ does not dominate these luminosities for the Milky Way either, but does contribute 10%–20% to these total luminosities (Cox & Laureijs 1989; Jackson et al. 1996). Extended emission contributes significantly to the CMZ’s IR and HCN luminosity.
2. We then investigate whether low-mass clumps can dominate L_{IR} or L_{HCN} in the Milky Way. While low-mass clumps do not contribute a significant fraction to L_{IR} , it is feasible that low-mass clumps can dominate L_{HCN} .
3. We also investigated whether subthermal HCN emission could dominate L_{HCN} . If the HCN detections from the Helfer & Blitz (1997) Galactic plane survey indeed represent subthermal emission of HCN, then subthermal HCN emission could dominate the total L_{HCN} . Our analysis of the Helfer & Blitz (1997) suggests that at least some of this HCN emission is not subthermal. Nevertheless, other observations suggest that there could be significant subthermal emission in both the Milky Way and other galaxies, and such emission could contribute significantly to a galaxy’s entire HCN emission.
4. Finally, we investigated whether extended IR emission can dominate L_{IR} . Based on analysis of the CMZ, the LMC, and previous studies, it appears that extended IR emission can dominate L_{IR} for a galaxy. Moreover, this extended emission does not appear to follow the Gao–Solomon relation.

Based on these results, it appears that extended IR emission probably dominates the total L_{IR} in galaxies. We are uncertain what dominates the HCN emission in galaxies, but we suggest low-mass star-forming clumps and/or subthermal emission could possibly dominate this emission. We discuss the implications of these results in Section 5.

4. EXTENDING THE COMPARISON BETWEEN THE IR AND DENSE GAS LUMINOSITY TO OTHER MOLECULES

In Figure 5 we present the relation between L_{IR} and L_{molecule} for the 12 molecular lines with significant numbers of detections by MALT90 (see Section 2.1). The four molecular lines most often detected, HCO^+ , HNC, N_2H^+ , and HCN (1–0), lie in the vicinity of the best-fit regression line for the Gao–Solomon relation. Therefore, galaxies may also follow a Gao–Solomon type relation using the tracers HCO^+ , HNC, and N_2H^+ . In general, datapoints for the other molecular lines (i.e., excluding HCO^+ , HNC, N_2H^+ , and HCN) have higher $L_{\text{IR}}/L_{\text{molecule}}$ ratios than that found by GS04. The datapoints for these molecular lines are expected to have higher ratios since they have similar critical densities but are significantly less abundant than HCN.⁷ In Table 2 we show the ordinary least squares (OLS) fits for $\log L_{\text{IR}}$ versus $\log L_{\text{molecule}}$ for all transitions except HN^{13}C , ^{13}CS , $\text{HNC}(4_{0,4}-3_{0,3})$, and CH_3CN (these transitions have four or less datapoints). The OLS regression was chosen over other regression fit algorithms because the uncertainties for each datapoint are not well determined. Moreover, using an OLS regression allows for a direct comparison to GS04 OLS fits. We test the behavior of the OLS regression for each line by using the random resampling with replacement bootstrapping technique (e.g., Simpson & Mayer-Hasselwander 1986). The bootstrap tests confirmed the uncertainties in the OLS fitted slope and intercept values and demonstrated that the OLS fit results are insensitive to uncertainties in source distances at the $\sim 30\%$ level. Fits from Wu05 and Wu10 exclude clumps with $L_{\text{IR}} < 10^{4.5} L_{\odot}$, but we do not provide these fits because there is a large spread in the data. Specifically, with the luminosity cut, the spread of the data for the y -axis (L_{IR}) becomes very similar to the spread of the x -axis (L_{molecule}) and thus regression dilution bias significantly reduces the OLS slope.

In Figure 6, we show the ratio $L_{\text{IR}}/L_{\text{molecule}}$ versus L_{IR} . $L_{\text{IR}}/L_{\text{molecule}}$ is independent of distance; therefore, this figure is similar to the F_{IR} versus F_{HCN} plot shown in Figure 2. Wu05 and Wu10 used a similar plot with their data to argue that $L_{\text{IR}}/L_{\text{HCN}}$ is constant for infrared luminosities $L_{\text{IR}} > 10^{4.5} L_{\odot}$. They argue that below $10^{4.5} L_{\odot}$ (approximately the luminosity of an H II region), there is a sudden drop in $L_{\text{IR}}/L_{\text{HCN}}$. We do not see a sudden drop off at this luminosity; instead, we see the general trend that more luminous (and likely higher mass) infrared clumps have excess L_{IR} per unit L_{HCN} as compared to the less luminous clumps. This is consistent with our interpretation in Section 3 suggesting that low-mass clumps have a significant excess L_{HCN} per unit L_{IR} . The trend may be due to the following: (1) More massive clumps are more likely to sample the high-mass regime of the IMF. Since the luminosity of stars scales with the third power of its mass, the dust of embedded clumps that host the most massive stars will absorb more luminosity which in turn will reemit in the infrared; (2) More massive clumps may have higher densities and thus the HCN may be optically thick, causing the luminosity to be suppressed; and/or (3) More infrared-luminous clumps are often H II regions, and these clumps typically have lower column densities than protostellar clumps (Guzmán et al. 2015). If these clumps are optically thin,

⁷ For $\text{C}_2\text{H } N=1-0$, we only integrate the transition listed in Table 1; adding all $N=1-0$ transitions would increase these luminosities considerably.

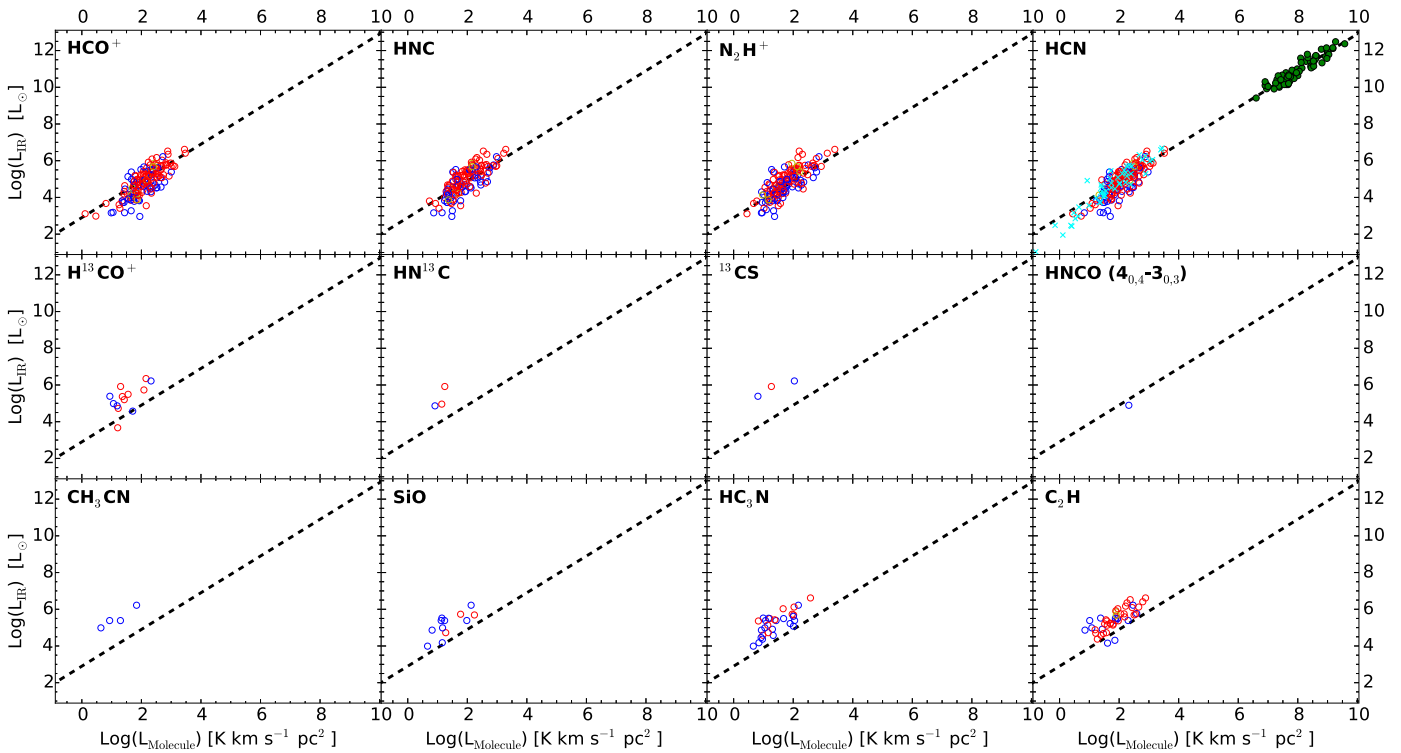


Figure 5. L_{IR} vs. L_{molecule} for twelve different MAL90 molecular lines. As identified using *Spitzer* near-IR images (Section 4.1), red circles indicate clumps classified as H II and Compact H II regions, blue circles indicate clumps classified as Protostellar, and yellow circles are clumps with other classifications. Green circles are galaxies from GS04 while cyan crosses are from Wu10. The dashed line shows the Gao–Solomon relation $\log L_{\text{IR}} = 1.00 \log L_{\text{molecule}} + 2.9$.

Table 2
IRAS Luminosity vs. Line Luminosity, all L_{IR} luminosities

Molecular Line	Slope	Intercept	R^2
HCO ⁺ (1–0)	1.16 ± 0.08	2.38 ± 0.17	0.60
HNC(1–0)	1.16 ± 0.08	2.64 ± 0.16	0.61
N ₂ H ⁺ (1–0)	1.13 ± 0.08	2.81 ± 0.14	0.61
HCN(1–0)	1.21 ± 0.07	2.32 ± 0.15	0.66
H ¹³ CO ⁺ (1–0)	0.99 ± 0.40	3.78 ± 0.62	0.36
SiO(2–1)	0.95 ± 0.27	3.85 ± 0.39	0.56
HC ₃ N(10–9)	0.93 ± 0.15	3.92 ± 0.23	0.57
C ₂ H(1–0) ^a	0.92 ± 0.12	3.72 ± 0.23	0.57

Notes. Format of regression fit is $\log(L_{\text{IR}}) = \text{Slope} \times \log(L_{\text{molecule}}) + \text{intercept}$. R^2 is the Pearson coefficient of determination.

^a See Table 1 for specific transition.

a deficit in HCN(1–0) luminosity would exist for a given infrared luminosity.

For the four brightest lines, HCO⁺, HNC, N₂H⁺, and HCN, the slope of the linear regression fit of $\log(L_{\text{IR}}/L_{\text{molecule}})$ versus $\log(L_{\text{IR}})$ is ~ 0.5 , indicating some correlation between L_{IR} and L_{molecule} . In other words, Figure 6 is not a plot of L_{IR} versus L_{IR} , which has an expected linear regression slope of 1.

In order to analyze the clump-scale Gao–Solomon relation in more detail, we plot the six lines with the most detections, HCO⁺, HNC, N₂H⁺, HCN, HC₃N, and C₂H, in Figure 7. In this Figure, we show the best-fit line for the Gao–Solomon relation and the linear regression fit for the MAL90 clumps. HCO⁺ and HCN lie slightly below the best-fit line for the Gao–Solomon relation while N₂H⁺ and HNC lie on top of the line.

A Kolmogorov–Smirnov test indicates that for MAL90 clumps, $L_{\text{IR}}/L_{\text{HCN}}$ and $L_{\text{IR}}/L_{\text{HCO}^+}$ could be drawn from the same distribution (P -value of 0.70), but $L_{\text{IR}}/L_{\text{HNC}}$ and $L_{\text{IR}}/L_{\text{N}_2\text{H}^+}$ likely come from a different distribution than $L_{\text{IR}}/L_{\text{HCN}}$ (P -values of less than 10^{-6}). The abundances and excitation parameters for these two molecular lines are not expected to be the exactly the same, and abundances of these lines can be affected by physical conditions of the region.

We also investigate the spread of the correlations between L_{IR} and the line luminosities for different molecules (L_{molecule}) in order to discern which molecule shows the tightest correlation. In Table 2 we show the tabulation of the coefficient of determination, R^2 , for each relation. Except for H¹³CO⁺, all lines with regression fits have similar R^2 values (~ 0.6) indicating that they all have a similar spread. In order to use a measurement that is less affected by outliers, we also plot the quantile regression fits (e.g., Koenker & Hallock 2001), for quantiles $q = 0.1, 0.3, 0.5, 0.7, \text{ and } 0.9$ in Figure 7 (where q is the expected fraction of data below the q quantile regression fit line). The dispersion of the quantile fits, particularly for the four brightest lines HCO⁺, HNC, N₂H⁺, and HCN, are very similar. These four brightest lines have a $L_{\text{IR}}/L_{\text{molecule}}$ difference of ~ 2 orders of magnitude between quantiles $q = 0.1$ and $q = 0.9$.

4.1. Clump Evolutionary Stage and the L_{IR} and L_{molecule} Relation

In the MAL90 catalog (J. Rathborne et al. 2016, in preparation), the evolutionary stage of each MAL90 clump has been classified based on visual inspection of mid-IR images from *Spitzer* IRAC and MIPS ($3.6\text{--}24 \mu\text{m}$, Benjamin

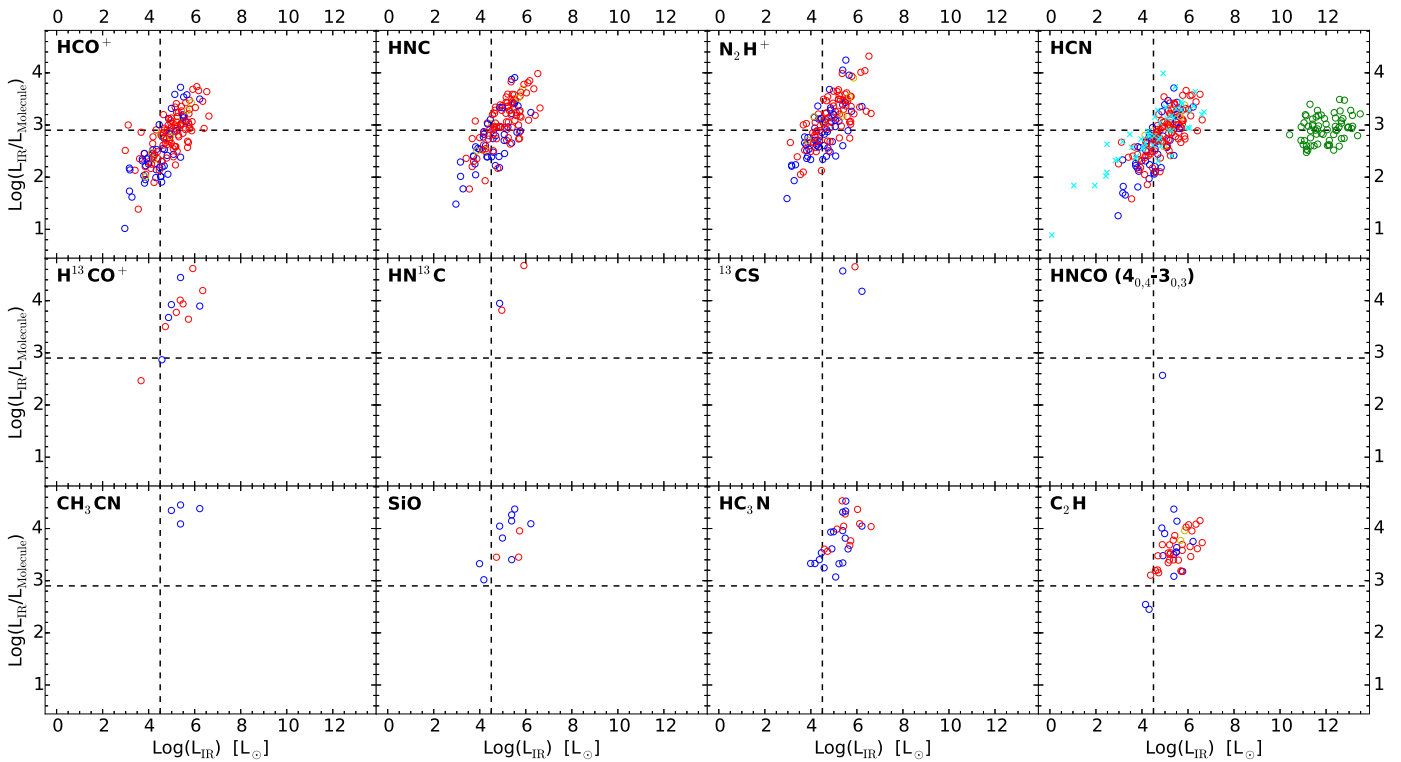


Figure 6. Distance-independent $L_{\text{IR}}/L_{\text{molecule}}$ vs. L_{IR} for different molecular lines. $L_{\text{IR}}/L_{\text{molecule}}$ are in units of L_{\odot} ($\text{K km s}^{-1} \text{pc}^2$) $^{-1}$. Colors and markings are the same as Figure 5. Dashed reference lines are shown for $L_{\text{IR}} = 10^{4.5} L_{\odot}$ (vertical line) and the average ratio for GS04 galaxies $L_{\text{IR}}/L_{\text{molecule}} = 10^{2.9} L_{\odot}$ ($\text{K km s}^{-1} \text{pc}^2$) $^{-1}$ (horizontal line). $L_{\text{IR}}/L_{\text{molecule}}$ decreases with decreasing L_{IR} . There appears no evidence of a definitive drop in L_{HCN} at a particular value of L_{IR} as proposed by Wu05 and Wu10.

et al. 2003; Carey et al. 2009). These clumps have been classified as Quiescent, Protostellar, Compact H II region, H II region, photodissociation region (PDR), or Uncertain. The classifications are indicated in Table 4. Details of the classification scheme are discussed in multiple MALT90 papers (e.g., Hoq et al. 2013; Jackson et al. 2013; Stephens et al. 2015). Since *IRAS* only detects the brightest clumps, the clumps analyzed in this paper are primarily those classified as Protostellar, Compact H II region, or H II region. Protostellar clumps have compact $24 \mu\text{m}$ emission and enhanced $4.5 \mu\text{m}$ emission (“green fuzzies,” Chambers et al. 2009). H II regions typically appear yellow in the three-color *Spitzer* images consisting of the 3.6, 8.0, and $24 \mu\text{m}$ bands. Compact H II regions are visually similar and smaller, which either indicates a less evolved or a more distant H II region. Since Compact H II regions are a type of H II region and comprise only a small sample of the total sample of clumps, we group these clumps with H II regions for all figures and the rest of the paper.

We indicate the evolutionary classes of each clump in the scatterplots of Figures 5–7. For the four brightest lines, HCO^+ , HNC, N_2H^+ , and HCN, there is an apparent trend based on the clump’s evolutionary stage; clumps classified as H II regions tend to be above the least-squares regression fit and clumps classified as Protostellar tend to be below. In Table 3 we show the fractions of each evolutionary stage above the fit and show the uncertainty, confirming that this trend is significant. For the low L_{IR} regime, the evolutionary stage of a clump has a clear impact on the relation between L_{IR} and L_{molecule} . This is expected because clumps containing H II regions will have hotter gas and dust than those containing protostellar sources.

Continuum flux is more dependent on the dust temperature ($F_d \propto T_d^{4+b}$, where the dust opacity index $b \approx 1-2$) than line flux is on the gas kinetic temperature ($F_g \propto T_k$), and at these high densities, $T_d \approx T_k$. However, this trend becomes less prominent for MALT90 clumps with $L_{\text{IR}} > 10^{4.5} L_{\odot}$. We visually inspect the *Spitzer* mid-IR for these particular clumps containing protostellar sources and find that these clumps are particularly bright sources. While early-B stars can also have high luminosities, these clumps could also contain hyper- or ultra-compact H II regions that are undetectable with *Spitzer*. Moreover, these clumps often have H II regions associated with the region that are within the *IRAS* beam. In other words, the Protostellar classification for the more infrared-luminous Protostellar clumps may in fact be H II regions.

5. DISCUSSION

In order to explain why the Gao–Solomon relation extends linearly over several orders of magnitude from galaxies to Galactic clumps, Wu05 proposed that $\sim 1 \text{ pc}$ sized dense clumps are the basic unit of star formation, and these dense clumps with $L_{\text{IR}} > 10^{4.5} L_{\odot}$ have a characteristic ratio $L_{\text{IR}}/L_{\text{HCN}}$ (where $L_{\text{HCN}} \propto M_{\text{dense}}$). They suggested that the observed $L_{\text{IR}}/L_{\text{HCN}}$ for a galaxy is a summation of large numbers of clumps. At the $\sim 1 \text{ pc}$ clump-scale, we question a characteristic value for the ratio $L_{\text{IR}}/L_{\text{HCN}}$ for the following reasons.

1. This interpretation requires approximately 10 times more high-mass star-forming clumps than are currently known in the Milky Way.

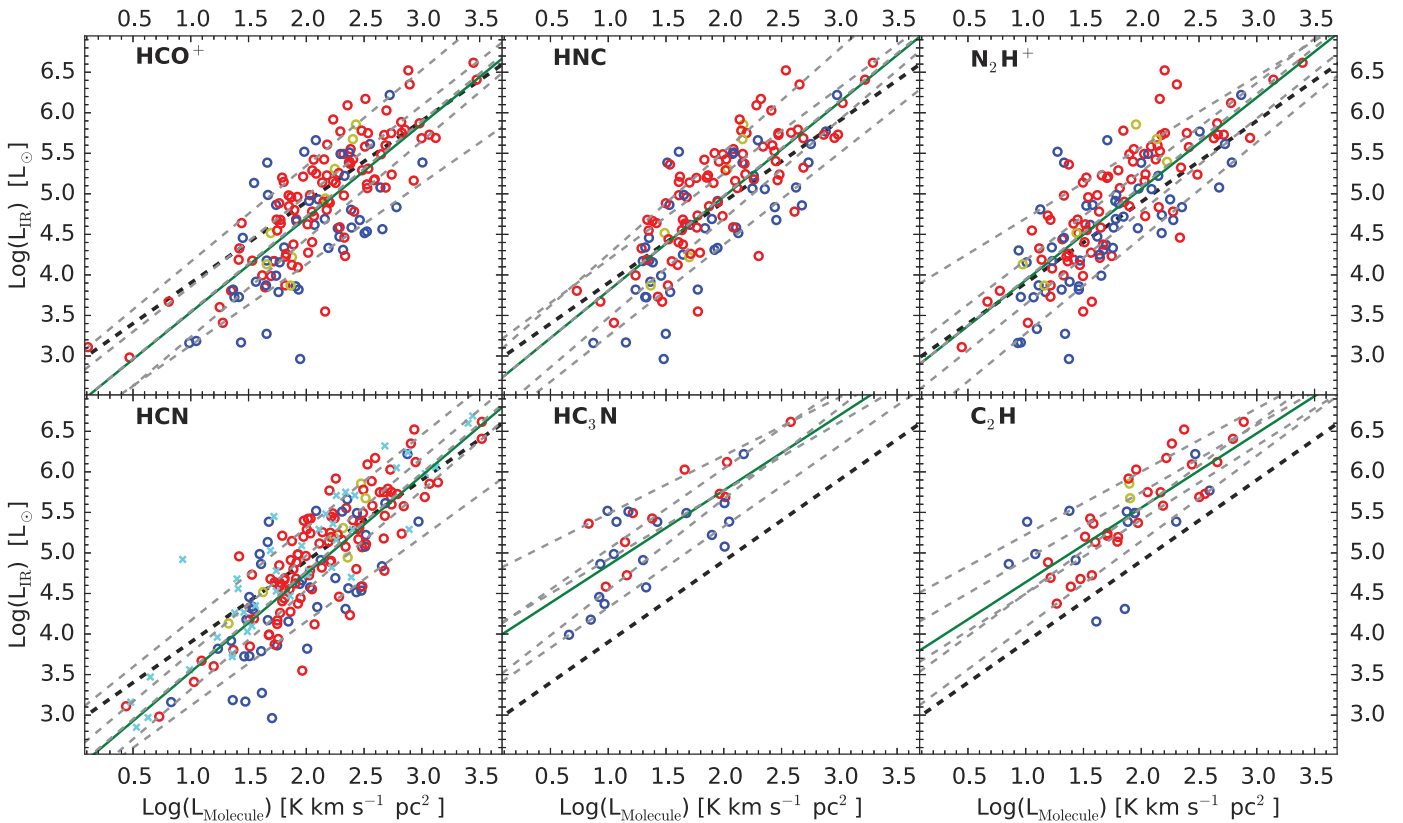


Figure 7. L_{IR} and L_{molecule} relation for the six molecular lines with the most MALT90 detections. Clumps classified as H II Region clumps (compact and not compact) and Protostellar clumps are shown in red and blue, respectively, while clumps with other classifications are shown in yellow. The black dashed line shows the fit to the GS04 sources. The green line shows the least squares fit for each molecular line for the MALT90 clumps. Five gray dashed lines show the quantile regression fits for quantiles (bottom to top line) $q = 0.1, 0.3, 0.5, 0.7,$ and 0.9 , respectively. Clumps from Wu10 for HCN are shown as cyan crosses and were not used in any of the fits.

Table 3

Fraction of Clumps above Regression Fit for Different Evolutionary Stages

Molecular Line	Clump Fraction above Regression Fit		
	H II Regions	Protostellar	Other
HCO ⁺ (1–0)	0.61 ± 0.05	0.33 ± 0.07	0.63 ± 0.17
HNC(1–0)	0.63 ± 0.05	0.30 ± 0.07	0.67 ± 0.19
N ₂ H ⁺ (1–0)	0.60 ± 0.05	0.35 ± 0.06	0.83 ± 0.15
HCN(1–0)	0.58 ± 0.05	0.39 ± 0.07	0.86 ± 0.13
HC ₃ N(10–9)	0.64 ± 0.15	0.44 ± 0.12	N/A
C ₂ H(1–0) ^a	0.47 ± 0.09	0.46 ± 0.14	N/A

Notes. Uncertainty in the percentages p were calculated via $\sqrt{p(1-p)/n}$ where n is the number of clumps containing a particular evolutionary stage. Percentages marked “N/A” had insufficient numbers to calculate a percentage and uncertainty.

^a See Table 1 for specific transition.

2. In many regions and perhaps over an entire galaxy, extended infrared emission can dominate over the infrared emission emitted from clumps, and the regions of extended emission do not follow the Gao–Solomon relation.
3. In the CMZ, the $L_{\text{IR}}/L_{\text{HCN}}$ ratio is a factor of 4 smaller than that suggested by the Gao–Solomon relation.
4. At the 1 pc clump-scale, there is a significant scatter in the plots for L_{IR} and L_{HCN} (and other molecules); the

difference between $L_{\text{IR}}/L_{\text{HCN}}$ for quantiles $q = 0.1$ and $q = 0.9$ (the middle 80% of the data) is approximately two orders of magnitude (Figure 7).

Based on these reasons, we suggest and will assume from hereon that $L_{\text{IR}}/L_{\text{HCN}}$ is not constant at the clump scale. The Gao–Solomon relation, however, demonstrates that a constant $L_{\text{IR}}/L_{\text{HCN}}$ exists on the ~ 10 kpc scales of the entire galaxies. The theoretical framework put forth by Kruijssen & Longmore (2014) suggests that due to incomplete sampling of independent star-forming regions, star formation relations such as the Gao–Solomon relation will no longer hold below some spatial scale. They suggest that the star formation relations will break down for normal spiral galaxies at size scales of approximately the Toomre length, which is approximately the separation between two spiral arms. If this theoretical framework is correct, then the scatter we find at the clump scale is expected.

Since $L_{\text{IR}}/L_{\text{HCN}}$ does not appear to be constant at the clump scale, at first glance it may be surprising that the Galactic clumps are scattered among the best fit for the Gao–Solomon relation. The entire Galaxy has significant infrared emission from hot, warm, and cold dust (Cox et al. 1986), and each clump is composed of different quantities of each, causing significant scatter for the luminosities of Galactic clumps. Therefore, high-mass clumps may be expected to lie scattered along the Gao–Solomon relation, with the median

clump reflecting the galaxy-scale characteristic ratio of $L_{\text{IR}}/L_{\text{HCN}}$.

An understanding of why the Gao–Solomon relation is constant at a galaxy-scale requires an understanding of the origin of the infrared and dense gas (as probed by HCN) luminosity. The vast majority of the infrared luminosity comes from reprocessed light generated by high-mass stars, regardless of whether the dust emission comes from regions of compact gas or more diffuse gas heated by the ISRF. All stars form in areas of dense gas, and these areas may dominate the luminosity of HCN. If the CIMF and IMF are both universal at some size-scale, such as the size-scale of a galaxy, integrating the IR and dense gas luminosities of stars and clumps predicted by these mass functions will cause the ratio $L_{\text{IR}}/L_{\text{HCN}}$ to be constant for the same size-scale. In other words, if the stellar and CIMFs vary from galaxy to galaxy, the ratio $L_{\text{IR}}/L_{\text{HCN}}$ is not expected to be constant for galaxy-scales. If both the CIMF and IMF are universal at some size-scale, the amount of dense gas from clumps that eventually forms stars must be constant at this size-scale as well, i.e., there is a constant dense gas star formation efficiency (SFE) at this scale. Since gas flows from clumps to cores (size-scale of ~ 0.1 pc) to stars, a universal CIMF, IMF, and SFE suggests that the core-mass function (CMF) must be universal at the same size-scale. We note that we have not proven that these SFE, IMF, CMF, and CIMF are universal, but suggest that our analysis is consistent with them being universal. Additionally, the universality may only be valid for the types of galaxies observed in **GS04**, i.e., normal spiral galaxies, LIRGs, and ULIRGs.

The spatial scale at which both the IMF and CIMF are universal has to be sufficiently large in order to sample large populations of high-mass stars and high-mass star-forming clumps. The size-scale must sample areas with cold, warm, and hot dust since all three significantly contribute to a galaxy’s total L_{IR} (Cox et al. 1986). Moreover, this size-scale needs to sample clumps of multiple stages of evolution since even the evolutionary state of a clump can affect the observed ratio of $L_{\text{IR}}/L_{\text{HCN}}$ (Section 4.1). This size-scale is certainly much larger than a clump (~ 1 pc). Even star formation activities within GMCs (size scales ~ 10 – 100 pc) can vary significantly from cloud to cloud (e.g., Fukui et al. 1999). Moreover, high-mass stars typically form in spiral arms, so the size scale where $L_{\text{IR}}/L_{\text{HCN}}$ is expected to be constant is probably larger than gaps between spiral arms (\sim kpc scale, e.g., Reid et al. 2014). We propose that the ratio $L_{\text{IR}}/L_{\text{HCN}}$ becomes constant at some scale larger than ~ 1 kpc because only this size-scale will contain enough clumps to completely sample the CIMF, IMF, and the distribution in their evolutionary states. The idea that the Gao–Solomon relation breaks down at some size-scale and depends on the star-forming region’s evolutionary stage is consistent with the theoretical framework put forth by Kruijssen & Longmore (2014).

The universality of the SFE, IMF, CMF, and CIMF might be questionable due to some scatter in the **GS04** plot; the tabulated $L_{\text{IR}}/L_{\text{HCN}}$ for each galaxy in **GS04** can vary by an order of magnitude. This scatter is partially due to the fact that the galaxies are subject to different physical conditions. We suggested in Section 3.1.1 that the physical conditions toward a galaxy’s center may be a source of this scatter. In general, the SFE, IMF, CMF, and CIMF may not be universal toward Galactic nuclei where the environments may be significantly

different (e.g., different levels of turbulence and whether the galaxy contains an active galactic nuclei). Galaxies can also be at different evolutionary stages or subject to different conditions (e.g., starbursts or mergers). Graciá-Carpio et al. (2008) found that $L_{\text{IR}}/L_{\text{HCN}}$ may be a factor of 2–3 higher in LIRGs and ULIRGs than in normal galaxies. This difference could be due to the fact that emission from high-density tracers can be self-absorbed toward the nuclei (few 100 pc scale) of LIRGs and ULIRGs (Aalto et al. 2015), and these nuclei contain a large fraction of these galaxies’ IR luminosity. Gao et al. (2007) found that in early universe ($2 < z < 6.5$) emission-line galaxies (EMGs) are significantly offset from the Gao–Solomon relation, with a large excess of L_{IR} per unit of L_{HCN} . The galaxies in **GS04** all have $z < 0.1$ (and typically have $z < 0.01$), suggesting the star-forming properties of high-redshift galaxies may differ significantly from those of low-redshift galaxies. EMGs typically have lower metallicities⁸ (0.07 – $0.7 Z_{\odot}$ for $0.6 < z < 2.4$, Xia et al. 2012) which may account for the deficit of L_{HCN} compared to **GS04** galaxies. Metallicities of LIRGs and ULIRGs can also vary significantly, from ~ 0.3 to $2.8 Z_{\odot}$, with typical values ~ 1.0 – $1.25 Z_{\odot}$ (Rupke et al. 2008). While metallicity differences are not expected to affect the IMF (Bastian et al. 2010 and references therein), they certainly affect the abundances of high-density tracers like HCN due to increased photoionization of the molecules from a stronger radiation field (e.g., Bolatto et al. 1999) and the availability of metals. On the other hand, large grains, the primary emitters for *IRAS* bands, are more resilient to destruction for a given radiation field (e.g., Stephens et al. 2014). In short, just as clumps are subject to different conditions within the Milky Way, external galaxies are also subject to different conditions which could be the source of scatter for $L_{\text{IR}}/L_{\text{HCN}}$ in **GS04**.

Since clumps do not appear to have a specific $L_{\text{HCN}}/L_{\text{IR}}$ ratio as proposed by Wu05 and Wu10, a different explanation is needed for the reason that L_{IR} versus $L_{\text{CO}(1-0)}$ follows a different power-law relation than L_{IR} versus $L_{\text{HCN}(1-0)}$. Narayanan et al. (2008) considered a galaxy that follows the Schmidt law (Schmidt 1959), i.e., the star formation rate (SFR, typically probed by L_{IR}) depends on the mean molecular gas mass density ρ according to

$$\text{SFR} \propto \rho^N. \quad (5)$$

In the Narayanan et al. (2008) simulations, which includes 3D non-local thermodynamic equilibrium radiative transfer calculations, the luminosity of the molecules (at least those considered in the simulations, i.e., CO and HCN), follow the power law

$$L_{\text{molecule}} \propto \rho^{\beta}, \quad (6)$$

where ρ is the mean molecular gas mass density in a grid cell of clouds along the line of sight. Given these two equations, the relation between SFR (as probed by L_{IR}) and L_{molecule} can be understood as

$$L_{\text{IR}} \propto \text{SFR} \propto L_{\text{molecule}}^{\alpha}, \quad (7)$$

where $\alpha = N/\beta$. Equation (5) is commonly assumed to behave according to the Schmidt index $N = 1.4$. Therefore, different values of β for different molecules reflect the power-law index

⁸ In order to calculate metallicity in units of Z_{\odot} , we assume $12 + (\text{O}/\text{H})_{\odot} = 8.66$ (Asplund et al. 2004) in this paper.

α observed across an entire galaxy. Narayanan et al. (2008) suggested that the value of β depends on the amount of diffuse gas emitting subthermally by molecules resonantly scattering photons emitted from dense regions. Typically CO(1–0) gas is above the critical density, causing there to be an insignificant emission from subthermal CO(1–0) gas. Therefore, the luminosity of CO will be directly proportional to the density, i.e., $\beta = 1$, and the SFR–line luminosity relation behaves according to the Schmidt index, i.e., $\alpha = N = 1.4$. However, high-density tracers such as HCN(1–0) have critical densities which are above the average number densities of a typical galaxy. Therefore, a large quantity of HCN(1–0) emitting gas will be diffuse, emitting subthermally. The simulations from Narayanan et al. (2008) suggested that emission from thermally emitting dense clumps can be absorbed by diffuse gas and re-emitted subthermally. The diffuse HCN(1–0) gas will have a higher luminosity per unit density since the photons originate from thermal emission of dense regions. Therefore, the $L_{\text{molecule}}-\rho$ relation will be superlinear, i.e., $\beta > 1$, causing α to be less than the Schmidt index. HCN appears to have $\beta = N$ causing $\alpha = 1$. Other lines can have a variety of values of β (larger than 1), allowing for the possibility of α to have a value of less than 1. α values of sub-unity have been found for galaxies using higher- J transitions (Baan et al. 2008; Busmann et al. 2008; Graciá-Carpio et al. 2008; Juneau et al. 2009) in accordance with the predictions of Narayanan et al. (2008). Nevertheless, Zhang et al. (2014) observed even higher- J transitions with APEX, specifically HCN(4–3), HCO⁺(4–3), and CS(7–6), and found values of α near unity, disagreeing with Narayanan et al. (2008).

Our analysis in Section 3.1.3 suggests significant subthermal emission of high-density tracers within the Milky Way and other galaxies. This emission may cause β to be larger than 1. Therefore, our observations are consistent with the simulations of Narayanan et al. (2008). Nevertheless, we are unable to confirm that $\beta = N$ and that a significant amount of diffuse HCN emission arises from resonant scattering of photons originally produced in dense clumps.

6. SUMMARY

We use molecular line data from clumps (~ 1 pc scale) from the MALT90 survey, and, along with other publications and ancillary data, we investigate the Gao–Solomon relation for HCN and the L_{IR} versus L_{molecule} relation for 11 other molecular lines. We reach the following conclusions.

- (1) We reject the Wu05 idea that clumps have a specific $L_{\text{IR}}/L_{\text{HCN}}$ ratio (with small scatter) for clumps $> 10^{4.5} L_{\odot}$. The ratio $L_{\text{IR}}/L_{\text{HCN}}$ is probably not constant at the clump-scale, but is constant at some larger scale. We propose that the scale in which $L_{\text{IR}}/L_{\text{HCN}}$ is expected to be constant is $\gtrsim 1$ kpc.
- (2) High-mass star-forming clumps likely account for only $\sim 10\%$ of an entire galaxy’s L_{IR} and L_{HCN} . Much of the IR emission comes from dust heated by the ISRF. The dominant source of a galaxy’s L_{HCN} is uncertain, but we suggest that low-mass star-forming clumps or subthermal emission may dominate the HCN emission.
- (3) Our analysis is consistent with the models set forth by Krumholz & Thompson (2007) and Narayanan et al.

(2008) that suggest that the relation $L_{\text{IR}} \propto L_{\text{molecule}}^{\alpha}$ depends on how the molecular line’s critical density compares with the median density of star-forming clouds in a galaxy. For lines with critical density significantly above the median density of a galaxy, a significant amount of photons are redistributed from thermal gas to subthermal gas, causing α to be smaller than the Schmidt index of $N = 1.4$.

- (4) The fact that $L_{\text{IR}}/L_{\text{HCN}}$ is only expected to have the same characteristic value of galaxies at large scales is consistent with the idea that spiral galaxies have a universal star formation efficiency, IMF, core mass function, and CIMF. While the universality can be questioned at small scales, they are likely universal at some large scale, which we suggest to be $\gtrsim 1$ kpc.
- (5) The CMZ adds significant luminosity to the entire Milky Way’s L_{IR} and L_{HCN} , but the CMZ does not lie on the best-fit line of the Gao–Solomon relation. This is likely due to the fact that the CMZ is subject to different conditions, e.g., extremely high turbulence, as compared to the rest of the galaxy. Differences in the contribution of other galaxies’ CMZ to the global HCN and IR luminosities could be a source of scatter for the Gao–Solomon relation.
- (6) We investigate the Galactic clump relation between L_{IR} and L_{molecule} for molecules other than HCN. A positive correlation exists between L_{IR} and L_{molecule} for each molecule, and we find no sudden drop in the ratio of $L_{\text{IR}}/L_{\text{molecule}}$ for $L_{\text{IR}} < 10^{4.5} L_{\odot}$. We find that the $L_{\text{IR}}/L_{\text{HCN}}$ ratios are the most similar to $L_{\text{IR}}/L_{\text{HCO}^+}$ ratios.
- (7) The evolutionary stage of a clump, particularly for clumps with lower infrared luminosities, helps to predict whether a clump will have a higher or lower $L_{\text{IR}}/L_{\text{HCN}}$ ratio than expected from the Gao–Solomon relation. Specifically, protostellar sources are more likely to have a lower $L_{\text{IR}}/L_{\text{HCN}}$ ratio than H II regions.

In short, this paper finds that the Gao–Solomon relation is not likely explained as a summation of high-mass star-forming clumps. The relation could be explained by a universal star formation efficiency, IMF, core mass function, and CIMF. The size-scale at which $L_{\text{IR}}/L_{\text{HCN}}$ becomes a constant value must be much larger than the clump-scale. Future observations that map entire galaxies with high-density tracers at sub-kpc resolution will determine this size-scale.

We thank Mark Reid for pointing out the large amount of high-mass clumps that would be required to account for the global Galactic HCN and IR luminosities. This work was supported by NASA grant NNX12AE42G and NSF grant AST-1211844. A.E.G. acknowledges support from FONDECYT grant 3150570. This research made use of APLpy, an open-source plotting package for Python hosted at <http://aplpy.github.com>.

APPENDIX

TABLE OF FLUXES FOR EACH MOLECULAR LINE

Table 4 provides information for each of the MALT90 clumps that were analyzed in this paper. Specifically, this table includes information on each clump’s evolutionary classification, kinematic distance (if known), infrared flux, and up to 12 different molecular line fluxes.

Table 4
IR and Molecular Fluxes

ATLASGAL ^a Source	Mid-IR ^b Classification	D^c (kpc)	F_{IR} log Scale ($L_{\odot} \text{ kpc}^{-2}$)	F_{HCO^+}	F_{HNC}	$F_{\text{N}_2\text{H}^+}$	F_{HCN}	$F_{\text{H}^{13}\text{CO}^+}$	$F_{\text{HN}^{13}\text{C}}$	$F_{^{13}\text{CS}}$	$F_{\text{HNCO } 40,4}$	$F_{\text{CH}_3\text{CN}}$	F_{SiO}	$F_{\text{HC}_3\text{N}}$	$F_{\text{C}_2\text{H}}$
log Scale ($\text{K km s}^{-1} \text{ pc}^2 \text{ kpc}^{-2}$)															
AGAL000.166-00.446_S	H II Region	...	2.58	0.54
AGAL000.281-00.482_S	H II Region	...	3.43	0.96	0.75	0.60	0.95
AGAL000.316-00.201_S	H II Region	...	3.91	1.13	0.82	0.62	1.10	0.01	0.47
AGAL000.496+00.187_S	H II Region	...	3.39	0.54	0.17
AGAL000.526+00.182_S	H II Region	...	3.41	0.10	0.12	0.22	0.24	0.25
AGAL000.631+00.604_S	PDR	...	2.79	-0.22
AGAL000.666-00.034_A	Protostellar	...	4.75	1.62	1.38	...	1.80	0.22	0.75	0.72	0.63	...	0.27
AGAL000.666-00.034_B	Protostellar	...	4.75	0.70	0.69	0.61	...	1.10	...	1.44	1.08
AGAL000.769-00.249_A	H II Region	...	2.54	-0.18	0.26	0.35	-0.48
AGAL000.769-00.249_B	H II Region	...	2.54

Notes.

^a ATLASGAL clumps have either _S, _A, or _B after their names, as per J. Rathborne et al. (2016, in preparation). Those with the nomenclature _S are not likely to have multiple clumps along the line of sight. Those with _A and _B are likely to have confusion along the line of sight (i.e., they have two velocity components separated by $>15 \text{ km s}^{-1}$). For all numbers, fits, and figures within the bulk of the paper, _A and _B components are not used since the *IRAS* continuum contributed to each the _A and _B components cannot be deduced. We report the fluxes here for completeness.

^b Classification based on *Spitzer* three-color images (see Section 4.1).

^c Distances are kinematic distances from J. Whitaker et al. (2016, in preparation).

^d AGAL344.582-00.024_S and AGAL346.418+00.279_S fitting results were not used in this paper because the distances are unrealistically close for H II regions.

(This table is available in its entirety in machine-readable form.)

REFERENCES

- Aalto, S., Martín, S., Costagliola, F., et al. 2015, *A&A*, **584**, A42
- Aravena, M., Hodge, J. A., Wagg, J., et al. 2014, *MNRAS*, **442**, 558
- Asplund, M., Grevesse, N., Sauval, A. J., Allende Prieto, C., & Kiselman, D. 2004, *A&A*, **417**, 751
- Baan, W. A., Henkel, C., Loenen, A. F., Baudry, A., & Wiklind, T. 2008, *A&A*, **477**, 747
- Bastian, N., Covey, K. R., & Meyer, M. R. 2010, *ARA&A*, **48**, 339
- Battisti, A. J., & Heyer, M. H. 2014, *ApJ*, **780**, 173
- Benjamin, R. A., Churchwell, E., Babler, B. L., et al. 2003, *PASP*, **115**, 953
- Bolatto, A. D., Jackson, J. M., & Ingalls, J. G. 1999, *ApJ*, **513**, 275
- Bussmann, R. S., Narayanan, D., Shirley, Y. L., et al. 2008, *ApJL*, **681**, L73
- Carey, S. J., Noriega-Crespo, A., Mizuno, D. R., et al. 2009, *PASP*, **121**, 76
- Chambers, E. T., Jackson, J. M., Rathborne, J. M., & Simon, R. 2009, *ApJS*, **181**, 360
- Combes, F. 1991, *ARA&A*, **29**, 195
- Contreras, Y., Schuller, F., Urquhart, J. S., et al. 2013, *A&A*, **549**, A45
- Cox, P., Kruegel, E., & Mezger, P. G. 1986, *A&A*, **155**, 380
- Cox, P., & Laureijs, R. 1989, in Proc. IAU Symp. 136, Center of the Galaxy, ed. M. Morris (Dordrecht: Kluwer), 121
- Csengeri, T., Urquhart, J. S., Schuller, F., et al. 2014, *A&A*, **565**, 75
- Dzib, S., Loinard, L., Mioduszewski, A. J., et al. 2010, *ApJ*, **718**, 610
- Elmegreen, B. G., & Falgarone, E. 1996, *ApJ*, **471**, 816
- Feast, M. 1999, in IAU Symp. 190, New Views of the Magellanic Clouds, ed. Y.-H. Chu, N. B. Suntzeff, J. E. Hesser, & D. A. Bohlender (Cambridge: Cambridge Univ. Press), 542
- Foster, J. B., Jackson, J. M., Barnes, P. J., et al. 2011, *ApJS*, **197**, 25
- Foster, J. B., Rathborne, J. M., Sanhueza, P., et al. 2013, *PASA*, **30**, 38
- Fukui, Y., Kawamura, A., Minamidani, T., et al. 2008, *ApJS*, **178**, 56
- Fukui, Y., Mizuno, N., Yamaguchi, R., et al. 1999, *PASJ*, **51**, 745
- Gao, Y., Carilli, C. L., Solomon, P. M., & Vanden Bout, P. A. 2007, *ApJL*, **660**, L93
- Gao, Y., & Solomon, P. M. 2004, *ApJ*, **606**, 271
- Graciá-Carpio, J., García-Burillo, S., Planesas, P., Fuente, A., & Usero, A. 2008, *A&A*, **479**, 703
- Gruendl, R. A., & Chu, Y.-H. 2009, *ApJS*, **184**, 172
- Guzmán, A. E., Sanhueza, P., Contreras, Y., et al. 2015, *ApJ*, **815**, 130
- Helfer, T. T., & Blitz, L. 1997, *ApJ*, **478**, 233
- Hoq, S., Jackson, J. M., Foster, J. B., et al. 2013, *ApJ*, **777**, 157
- Jackson, J. M., Heyer, M. H., Paglione, T. A. D., & Bolatto, A. D. 1996, *ApJL*, **456**, L91
- Jackson, J. M., Rathborne, J. M., Foster, J. B., et al. 2013, *PASA*, **30**, 57
- Jones, P. A., Burton, M. G., Cunningham, M. R., et al. 2012, *MNRAS*, **419**, 2961
- Juneau, S., Narayanan, D. T., Moustakas, J., et al. 2009, *ApJ*, **707**, 1217
- Kennicutt, R. C., Jr. 1998a, *ARA&A*, **36**, 189
- Kennicutt, R. C., Jr. 1998b, *ApJ*, **498**, 541
- Koenker, R., & Hallock, K. F. 2001, *Journal of Economic Perspectives*, **15**, 143
- Kramer, C., Stutzki, J., Rohrig, R., & Corneliussen, U. 1998, *A&A*, **329**, 249
- Kroupa, P. 2001, *MNRAS*, **322**, 231
- Kruijssen, J. M. D., & Longmore, S. N. 2014, *MNRAS*, **439**, 3239
- Krumholz, M. R., & Thompson, T. A. 2007, *ApJ*, **669**, 289
- Lada, C. J., Forbrich, J., Lombardi, M., & Alves, J. F. 2012, *ApJ*, **745**, 190
- Ladd, N., Purcell, C., Wong, T., & Robertson, S. 2005, *PASA*, **22**, 62
- Lee, K. I., Fernández-López, M., Storm, S., et al. 2014, *ApJ*, **797**, 76
- Longmore, S. N., Bally, J., Testi, L., et al. 2013, *MNRAS*, **429**, 987
- Longmore, S. N., Rathborne, J., Bastian, N., et al. 2012, *ApJ*, **746**, 117
- Lucke, P. B., & Hodge, P. W. 1970, *AJ*, **75**, 171
- McQuinn, K. B. W., Simon, R., Law, C. J., et al. 2002, *ApJ*, **576**, 274
- Meixner, M., Panuzzo, P., Roman-Duval, J., et al. 2013, *AJ*, **146**, 62
- Mezger, P. G., Mathis, J. S., & Panagia, N. 1982, *A&A*, **105**, 372
- Narayanan, D., Cox, T. J., Shirley, Y., et al. 2008, *ApJ*, **684**, 996
- Narayanan, D., Groppi, C. E., Kulesa, C. A., & Walker, C. K. 2005, *ApJ*, **630**, 269
- Olmi, L., & Testi, L. 2002, *A&A*, **392**, 1053
- Papadopoulos, P. P. 2007, *ApJ*, **656**, 792
- Pekruhl, S., Preibisch, T., Schuller, F., & Menten, K. 2013, *A&A*, **550**, A29
- Reid, M. A., Wadsley, J., Petitclerc, N., & Sills, A. 2010, *ApJ*, **719**, 561
- Reid, M. A., & Wilson, C. D. 2006, *ApJ*, **650**, 970
- Reid, M. J., Menten, K. M., Brunthaler, A., et al. 2014, *ApJ*, **783**, 130
- Rupke, D. S. N., Veilleux, S., & Baker, A. J. 2008, *ApJ*, **674**, 172
- Salpeter, E. E. 1955, *ApJ*, **121**, 161
- Sanders, D. B., & Mirabel, I. F. 1996, *ARA&A*, **34**, 749
- Schmidt, M. 1959, *ApJ*, **129**, 243
- Schmidt, M. 1963, *ApJ*, **137**, 758
- Schneider, N., & Brooks, K. 2004, *PASA*, **21**, 290
- Schuller, F., Menten, K. M., Contreras, Y., et al. 2009, *A&A*, **504**, 415
- Seale, J. P., Meixner, M., Sewilo, M., et al. 2014, *AJ*, **148**, 124
- Simpson, G., & Mayer-Hasselwander, H. 1986, *A&A*, **162**, 340
- Solomon, P. M., Downes, D., & Radford, S. J. E. 1992, *ApJL*, **387**, L55
- Stephens, I. W., Evans, J. M., Xue, R., et al. 2014, *ApJ*, **784**, 147
- Stephens, I. W., Jackson, J. M., Sanhueza, P., et al. 2015, *ApJ*, **802**, 6
- Urquhart, J. S., Csengeri, T., Wyrowski, F., et al. 2014, *A&A*, **568**, A41
- van der Marel, R. P., & Cioni, M.-R. L. 2001, *AJ*, **122**, 1807
- Wu, J., Evans, N. J., II, Gao, Y., et al. 2005, *ApJL*, **635**, L173
- Wu, J., Evans, N. J., II, Shirley, Y. L., & Knez, C. 2010, *ApJS*, **188**, 313
- Xia, L., Malhotra, S., Rhoads, J., et al. 2012, *AJ*, **144**, 28
- Zhang, Z.-Y., Gao, Y., Henkel, C., et al. 2014, *ApJL*, **784**, L31
- Zinnecker, H., & Yorke, H. W. 2007, *ARA&A*, **45**, 481